SPECIAL
Process-Oriented Model Diagnostics
COLLECTION

ⓐConvective Transition Statistics over Tropical Oceans for Climate Model Diagnostics: GCM Evaluation⌀

Yi-Hung Kuo,[a] J. David Neelin,[a] Chih-Chieh Chen,[b] Wei-Ting Chen,[c] Leo J. Donner,[d]
Andrew Gettelman,[b] Xianan Jiang,[e] Kuan-Ting Kuo,[c] Eric Maloney,[f] Carlos R. Mechoso,[a]
Yi Ming,[d] Kathleen A. Schiro,[a,g] Charles J. Seman,[d] Chien-Ming Wu,[c] and Ming Zhao[d]

[a] *Department of Atmospheric and Oceanic Sciences, University of California, Los Angeles, Los Angeles, California*
[b] *National Center for Atmospheric Research, Boulder, Colorado*
[c] *Department of Atmospheric Sciences, National Taiwan University, Taipei, Taiwan*
[d] *Geophysical Fluid Dynamics Laboratory, Princeton, New Jersey*
[e] *Joint Institute for Regional Earth System Science and Engineering, University of California, Los Angeles, Los Angeles, California*
[f] *Department of Atmospheric Science, Colorado State University, Fort Collins, Colorado*

ABSTRACT

To assess deep convective parameterizations in a variety of GCMs and examine the fast-time-scale convective transition, a set of statistics characterizing the pickup of precipitation as a function of column water vapor (CWV), PDFs and joint PDFs of CWV and precipitation, and the dependence of the moisture–precipitation relation on tropospheric temperature is evaluated using the hourly output of two versions of the GFDL Atmospheric Model, version 4 (AM4), NCAR CAM5 and superparameterized CAM (SPCAM). The 6-hourly output from the MJO Task Force (MJOTF)/GEWEX Atmospheric System Study (GASS) project is also analyzed. Contrasting statistics produced from individual models that primarily differ in representations of moist convection suggest that convective transition statistics can substantially distinguish differences in convective representation and its interaction with the large-scale flow, while models that differ only in spatial–temporal resolution, microphysics, or ocean–atmosphere coupling result in similar statistics. Most of the models simulate some version of the observed sharp increase in precipitation as CWV exceeds a critical value, as well as that convective onset occurs at higher CWV but at lower column RH as temperature increases. While some models quantitatively capture these observed features and associated probability distributions, considerable intermodel spread and departures from observations in various aspects of the precipitation–CWV relationship are noted. For instance, in many of the models, the transition from the low-CWV, nonprecipitating regime to the moist regime for CWV around and above critical is less abrupt than in observations. Additionally, some models overproduce drizzle at low CWV, and some require CWV higher than observed for strong precipitation. For many of the models, it is particularly challenging to simulate the probability distributions of CWV at high temperature.

ⓐ Denotes content that is immediately available upon publication as open access.

⌀ Supplemental information related to this paper is available at the Journals Online website: https://doi.org/10.1175/JAS-D-19-0132.s1.

[g] Current affiliation: Jet Propulsion Laboratory, California Institute of Technology, Pasadena, California.

Corresponding author: Yi-Hung Kuo, yhkuo@atmos.ucla.edu

1. Introduction

Simulating deep convection in GCMs has been a longstanding challenge despite progress in computer power and model complexity. The tropical precipitation simulated by GCMs is often at odds with the observed and targeted studies have identified limitations of simulated convection as a likely contributor to major biases in climatology and large-scale modes of tropical variability—for example, the MJO (Del Genio et al. 2012; Zhu and Hendon 2015; Jiang 2017), the diurnal cycle of precipitation (Del Genio and Wu 2010; Rio et al. 2009; Hourdin et al. 2013; Covey et al. 2016), and the double

ITCZ (Mapes and Neale 2011; Hwang and Frierson 2013; Oueslati and Bellon 2013; Hirota et al. 2014). Tropical precipitation also exhibits great intermodel spread in the context of future change projection (Biasutti and Sobel 2009; Biasutti 2013; Voigt et al. 2016; Su et al. 2017; Maloney et al. 2019a). As a result, model diagnostic efforts targeting deep convection are central to several model improvement efforts across scales. Recent approaches seek process-oriented diagnostics that target improvements to physical parameterizations by investigating coordinated statistics for relationships among variables aimed at giving insight into underlying processes (Eyring et al. 2019; Maloney et al. 2019b). Such efforts include, for example, diagnostics for moist static energy (MSE) variance budget analysis (Wing and Emanuel 2014), MJO propagation (Kim et al. 2014; Gonzalez and Jiang 2017), MJO midlatitude teleconnection (Henderson et al. 2017), ENSO-related SST anomalies for seasonal to interannual predictability (Annamalai et al. 2014), warm rain processes (Suzuki et al. 2015), and tropical cyclone simulations (Kim et al. 2018).

Here we focus on convective transition statistics that serve as model diagnostics for the parameterization of deep convection (Peters and Neelin 2006; Neelin et al. 2009; Kuo et al. 2018, hereafter KSN18). These statistics characterize the PDFs of column water vapor (CWV) for precipitating points, the pickup of precipitation as a function of CWV, and the dependence of the moisture–precipitation relation on tropospheric temperature. The moisture–precipitation relation is representative of the relation between observed deep convection and the buoyancy available for deep convection (Holloway and Neelin 2009; Schiro et al. 2016; Ahmed and Neelin 2018), applying to both mesoscale-organized and smaller-scale convection (Schiro et al. 2018; Schiro and Neelin 2019). The relationship to convective instability has been examined in a single GCM (Sahany et al. 2012, 2014; Kuo et al. 2017). Here we systematically evaluate the performance of multiple GCMs in simulating key features of tropical precipitation and deep convection with such diagnostics.

KSN18 has detailed observational aspects of the convective transition statistics over tropical oceans using satellite retrievals and ground-based measurements, providing a baseline. Here, the same set of statistics are compiled for three sets of high-frequency (hourly and 6 hourly) GCM output and compared to observations to address a fundamental question: whether these statistics can target specific processes and differentiate the relevant parameterization schemes adopted by each GCM, namely, deep convective parameterizations. The first set consists of hourly output from a pair of uncoupled GFDL Atmospheric Model, version 4 (AM4)

and AM4 modified to include multiple deep plumes. The second set, also hourly output, is from the uncoupled NCAR CAM5.3 and the superparameterized CAM (SPCAM), which share the same dynamic core but differ in representations of moist convection. These two pairs of model comparison demonstrate that the convective transition statistics can reveal model characteristics directly relevant to the moist convective representations in contrast to the conventional diagnostic metrics based on long-term climatology and variability. The third set consists of 6-hourly output from a subset of models participating in the MJO Task Force (MJOTF)/GEWEX Atmospheric System Study (GASS) multimodel comparison project on the Madden–Julian oscillation (Petch et al. 2011; Jiang et al. 2015; hereafter MJOTF/GASS), which further enables us to perform similar assessment but for a selection (16 models/configurations) of mainstream GCMs.

This manuscript is organized as follows. Section 2 describes the observational and model data. Section 3 briefly summarizes the observational aspects of the basic convective transition statistics, with the corresponding model comparisons in section 4. The joint PDFs of CWV and precipitation, and the derived statistics, are presented in section 5. Summary and conclusions are given in section 6.

2. Data and model descriptions

a. Observational datasets

Compiling the desired statistics requires the CWV, precipitation rate P, and 1000–200-hPa column-integrated saturation humidity $\widehat{q_{sat}}$ $\{\widehat{q_{sat}} \equiv \int q_{sat}[T(p),p]dp/g$, where $q_{sat}[T(p),p]$ is the saturation specific humidity with respect to liquid water. Here, $\widehat{q_{sat}}$ is used as the bulk measure of tropospheric temperature (see KSN18 for comparison to vertically averaged tropospheric temperature).

To be consistent with previous studies, the 6-hourly 2.5° NCEP–DOE Reanalysis-2 temperature (Kanamitsu et al. 2002) is adopted for calculating $\widehat{q_{sat}}$ with interpolation as needed. Newer reanalysis products (e.g., ERA-Interim) give similar results (not shown). Our primary source of CWV and P is the TRMM Microwave Imager (TMI) retrievals processed by Remote Sensing Systems (version 7.1; TMIv7.1 hereafter; Wentz et al. 2015) for the period from 1 June 2002 through 31 May 2014. The TMIv7.1 data contain gridded (0.25°) snapshots of CWV and P (at 0.3-mm and 0.1 mm h^{-1} increments, respectively) over ocean. The CWV is capped at 75 mm and often records missing values in the presence of heavy precipitation (with increasing probability of missing

values starting around $P = 2\,\mathrm{mm\,h^{-1}}$ and recording almost nothing above $9\,\mathrm{mm\,h^{-1}}$). We gap fill the missing values using the available values at the nearest pixel to restore substantial coverage, but one should not overlook the uncertainty associated with the CWV counts at high P (see KSN18 for sensitivity to gap filling). The TMIv7.1 P exhibits a spurious cutoff around $10\,\mathrm{mm\,h^{-1}}$. Thus, for studying the PDFs of P, the TRMM Precipitation Radar (PR) 2A25 (v7; TRMM 2011) rainfall rate containing snapshots of P at ~5-km resolution is utilized. At its native resolution, the lowest value the PR can distinguish is ~$0.11\,\mathrm{mm\,h^{-1}}$.

b. Model descriptions

Part of the model data analyzed here are from the time-slice experiments performed by the NOAA Modeling, Analysis, Predictions and Projections (MAPP) Model Diagnostic Task Force (Maloney et al. 2019b), which include 2-yr-long high-frequency output under the AMIP settings. The relevant data consist of hourly snapshots of temperature and humidity, for calculating $\widehat{q_{\mathrm{sat}}}$ and CWV, and hourly average precipitation. The available models include uncoupled ~1° GFDL AM4 (Zhao et al. 2018a,b; AM4G9 hereafter), and AM4 modified to include multiple deep plumes and convective mesoscale circulations (Donner et al. 2011; AM4B6), and the uncoupled ~1° NCAR CAM5.3 (Neale et al. 2012). The two AM4 configurations, running through 2009–10, primarily differ in the convective parameterizations—double-plume convective scheme (Zhao et al. 2009) for AM4G9 versus Donner convective scheme (Donner 1993) for AM4B6—with associated tuning differences, but otherwise share most model components.

The CAM5.3, running through 1990–91, uses the Zhang–McFarlane deep convective parameterization (Zhang and McFarlane 1995) as updated by Neale et al. (2008) and Richter and Rasch (2008). For comparison, our analysis also includes another set of 10-yr-long hourly output from the uncoupled ~2° SPCAM [the atmospheric component of the superparameterized CESM (SP-CESM), version 1.1.1; prescribed monthly mean SST over 1982–2001], in which the moist convective processes are explicitly simulated by a 2D cloud-resolving model (Khairoutdinov and Randall 2003) instead of being parameterized. The SPCAM is run with the CAM4 physics. CAM5 (and CAM5.3) differs from CAM4 primarily in updated parameterization schemes and incorporating aerosol–cloud interactions, leaving most of the dynamic components unchanged. Thus, one major difference between the SPCAM and CAM5.3 lies in the representations of moist convection, which is expected to be the key difference for the statistics analyzed here.

To survey the convective transition in a variety of models, we also analyze the 6-hourly output of 16 models/configurations participating in the MJOTF/GASS Global Model Comparison Project, the 20-yr climate simulation component. Here, the precipitation is 6-hourly average, and all the data have been regridded to 2.5° × 2.5° resolution prior to our analysis (Jiang et al. 2015). This MJOTF/GASS ensemble further provides an opportunity for two case studies of the sensitivity of the convective transition statistics on (i) time-averaging and convective-cloud microphysics through two additional CAM5 instances [referred to as CAM5 and CAM5-ZM; see Section 4b(2) for more information on these instances], and on (ii) coupling/forcing configurations through three CNRM instances [CNRM-AM, CNRM-CM, and CNRM-ACM; Section 4b(3)].

See Table 1 and references therein for details regarding the examined models.

3. A summary of the observational aspects of convective transition statistics over tropical oceans

In this section, we briefly summarize the observed characteristics of convective transition over tropical oceans synthesized by KSN18.

Figures 1a–d show the basic statistics compiled using the TMIv7.1 data and Reanalysis-2 temperature at 1° resolution, including the conditionally averaged precipitation rate (conditional precipitation hereafter; calculated by including all events; Fig. 1a), conditional probability of precipitation ($P > 0.25\,\mathrm{mm\,h^{-1}}$; Fig. 1b), PDFs of CWV for all events (Fig. 1c) and for precipitating events (Fig. 1d), all as a function of CWV and $\widehat{q_{\mathrm{sat}}}$ for the tropical western Pacific (WPac; 20°S–20°N, west of 180°). Here, $\widehat{q_{\mathrm{sat}}}$ is used as a proxy for the bulk tropospheric temperature. The PDFs in Fig. 1c together represent the normalized joint distribution of CWV and $\widehat{q_{\mathrm{sat}}}$, reflecting the CWV–$\widehat{q_{\mathrm{sat}}}$ climatology in this basin. Multiplying these PDFs by the corresponding conditional probabilities in Fig. 1b leads to the PDFs for precipitating events in Fig. 1d.

The conditional precipitation and probability (Figs. 1a,b) sharply increase as CWV exceeds a certain threshold known as the critical CWV w_c (defined through Fig. 1e later); w_c increases with $\widehat{q_{\mathrm{sat}}}$. For low $\widehat{q_{\mathrm{sat}}}$ bins, the PDFs of CWV in Fig. 1c exhibit a characteristic shape, that is, a peak at low CWV below which the PDF drops sharply, and above which the PDF decreases slowly until reaching a cutoff around critical. As $\widehat{q_{\mathrm{sat}}}$ increases, another peak develops at high CWV around critical with the low-CWV peak diminishing. Neelin et al. (2009) has noted that low-CWV (high-CWV) events tend to occur

TABLE 1. Analyzed models with resolutions and references. Simulations 1–3 are provided by the NOAA MAPP MDTF time-slice experiments. Simulations 1–4 output hourly data. Simulations 5–20 are provided by the 20-yr climate simulation component of the MJOTF/GASS Global Model Comparison Project, with 6-hourly data regridded to 2.5° × 2.5° resolution. The descriptions of the MJOTF/GASS models follow Jiang et al. (2015, their Table 1).

	Model name	Institute	Resolution (lon × lat), vertical levels	References
1	AM4G9	Geophysical Fluid Dynamics	1.25° × 1°, L32	Zhao et al. (2018a,b)
2	AM4B6	Laboratory, NOAA	1.25° × 1°, L48	Zhao et al. (2018a,b)
3	CAM5.3	National Center for Atmospheric Research	1.25° × 0.9°, L30	Neale et al. (2012)
4	SPCAM	Colorado State University	GCM: 2.5° × 1.9°, L26 CRM: 4 km × 32 columns, L24	See note[a]
5	CAM5	National Center for Atmospheric Research	1.25° × 0.9°, L30	Neale et al. (2012)
6	CAM5-ZM	Lawrence Livermore National Laboratory	1.25° × 0.9°, L30	Song and Zhang (2011)
7	CNRM-AM	Centre National de la Recherche	T127 (1.4°), L31	Voldoire et al. (2013)
8	CNRM-CM	Scientifique/Météo-France		
9	CNRM-ACM			
10	EC-EARTH3	Rossby Center, Swedish Meteorological and Hydrological Institute	T255 (80 km), L91	See note[b]
11	BCC-AGCM2.1	Beijing Climate Center, China Meteorological Administration	T42 (2.8°), L26	Wu et al. (2010)
12	CanCM4	Canadian Centre for Climate Modeling and Analysis	2.8°, L35	Merryfield et al. (2013)
13	NavGEM1	U.S. Naval Research Laboratory	T359 (37 km), L42	See note[c]
14	MRI-AGCM3	Meteorological Research Institute, Japan	T159, L48	Yukimoto et al. (2012)
15	MIROC5	AORI/NIES/JAMSREC, Japan	T85 (1.5°), L40	Watanabe et al. (2010)
16	GISS-E2	Goddard Institute for Space Studies, NASA	2.5° × 2.0°, L40	Schmidt et al. (2014)
17	GEOS-5	Global Modeling and Assimilation Office, NASA	0.625° × 0.5°, L72	Molod et al. (2012)
18	CWB-GFS	Central Weather Bureau, Taiwan	T119 (1°), L40	Liou et al. (1997)
19	FGOALS-s2	Institute of Atmospheric Physics, Chinese Academy of Sciences	R42 (2.8° ×1.6°), L26	Bao et al. (2013)
20	ISUGCM	Iowa State University	T42 (2.8°), L18	Wu and Deng (2013)

[a] Here the SPCAM is the atmospheric component of the SP-CESM, version 1.1.1, in which the embedded CRM is the System for Atmospheric Modeling (SAM; Khairoutdinov and Randall 2003). For more regarding the SPCAM configuration for the examined simulation, see Kuo et al. (2019).

[b] Hazeleger et al. (2012) describes an earlier version of the EC-EARTH model, while here we have used a newer version based on ECMWF's IFS model cy36r4. The main differences between these model versions are an improved radiation scheme (Morcrette et al. 2008) and a new cloud microphysics (Forbes et al. 2012).

[c] The NAVGEM, version 1.0, model used here, for which there is no published reference, differs from NAVGEM 1.1 (Hogan et al. 2014) in that it lacks prognostic cloud water and that it uses the radiation scheme of Harshvardhan et al. (1987).

over ocean with colder (warmer SST), which is closely related to the locations of the descending (ascending) branches of the general circulation. Stechmann and Neelin (2011, 2014) have also demonstrated through a stochastic framework that the CWV PDFs are sensitive to processes like surface evaporation, precipitation, and moisture convergence. These observations suggest that the CWV PDFs are determined by the large-scale flow interacting with convective physics.

KSN18 noted that, because of the large spatial auto-correlation scales of temperature and CWV compared with that of precipitation, the conditional precipitation (Fig. 1a) and CWV PDF (Fig. 1c) are insensitive to the spatial resolution at which the statistics are compiled, while the conditional probability (Fig. 1b) and PDF of precipitating events (Fig. 1d) are more sensitive. It thus makes sense to define w_c through conditional precipitation alone so that it provides a resolution-independent metric. Following KSN18, we define w_c as the CWV value at which a linear fit for conditional precipitation (in the range 3–5 mm h^{-1}) intersects with the CWV axis. This is depicted in Fig. 1e, which shows the conditional precipitation as in Fig. 1a, but for 0.25° resolution and is collapsed by shifting CWV by w_c for each $\widehat{q_{sat}}$. Here, the resolution 0.25° is chosen instead of 1° to include more events, making the fitting numerically
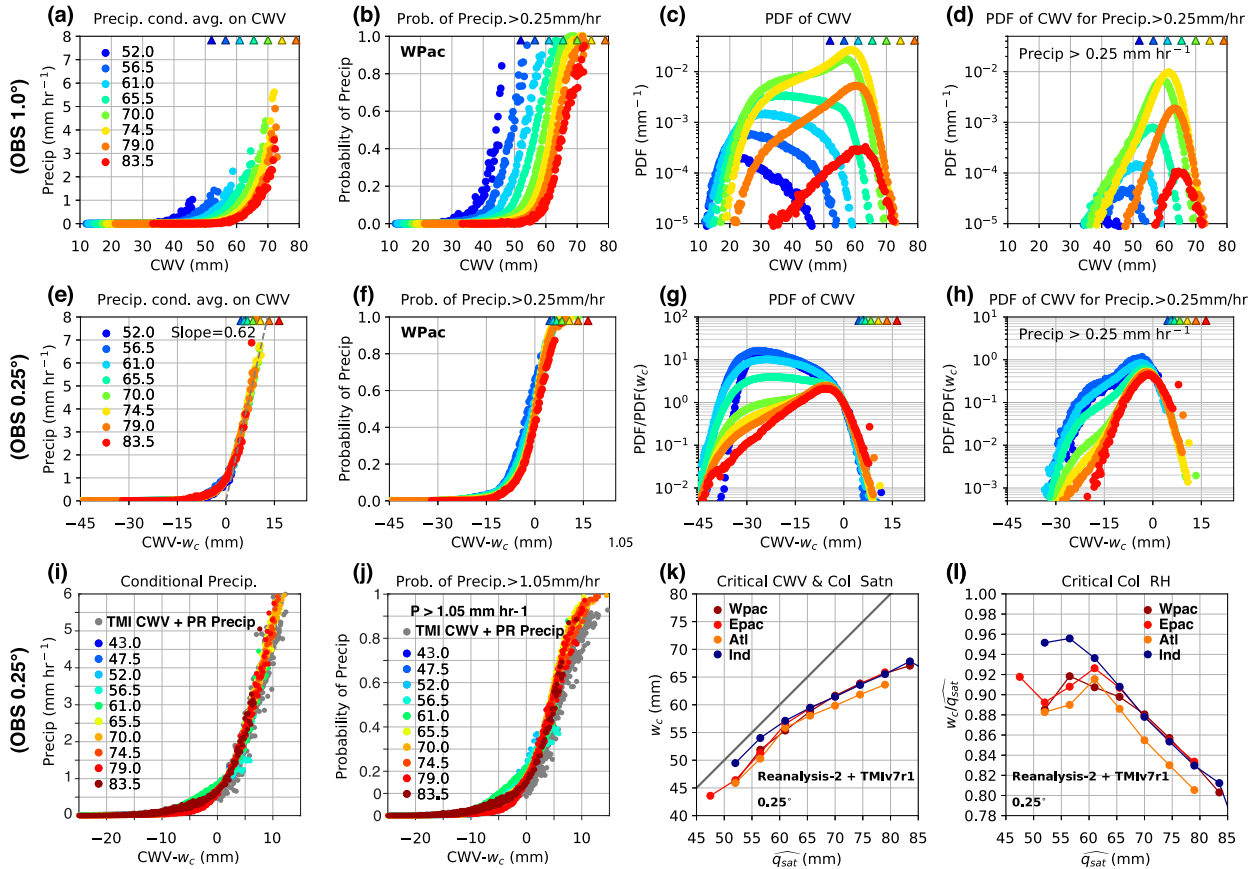
FIG. 1. (a) Conditionally averaged precipitation rate, (b) conditional probability of precipitation, (c) PDFs of all events, and (d) PDFs for precipitating events as a function of CWV and $\widehat{q_{sat}}$ (colors; mm) for the tropical western Pacific (20°S–20°N, west of 180°). In (a)–(d), results are using TMIv7.1 precipitation rate and CWV and Reanalysis-2 temperature compiled at 1° (colored markers). Triangles represent corresponding $\widehat{q_{sat}}$ values, which indicate where the column is approximately saturated, and underpopulated bins (PDF $< 10^{-5}$) are omitted. (e)–(h) As in (a)–(d), but at 0.25° to include more events, and with the statistics collapsed by shifting CWV for each $\widehat{q_{sat}}$ by the corresponding critical CWV w_c from (k), and with the PDFs scaled by values at w_c. (i) Collapsed conditionally averaged precipitation rate at 0.25° as in (e), but with data from three additional tropical (20°S–20°N) ocean basins (colored dots) and with TMIv7.1 precipitation rate replaced by PR 2A25 precipitation rate (gray dots). (j) As in (i), but for conditional probability of precipitation [$P > 1.05 \, \text{mm} \, \text{h}^{-1}$; different from the 0.25 mm h^{-1} threshold for (b) and (f)]. (k) Critical CWV w_c as a function of $\widehat{q_{sat}}$ for the four tropical ocean basins, with the gray line indicating the $\widehat{q_{sat}}$ value where the column is approximately saturated. (l) Critical column RH defined as $w_c/\widehat{q_{sat}}$. In (k) and (l), the values of w_c are calculated by fitting the conditionally averaged precipitation rate in the range 3–5 mm h^{-1} using TMIv7.1 data and Reanalysis-2 temperature compiled at 0.25°.

stable. The collapsed conditional probability and re-scaled CWV PDFs corresponding to those in Figs. 1b–d are shown in Figs. 1f–h, and the values of w_c and critical column RH $w_c/\widehat{q_{sat}}$ in Figs. 1k and 1l.

From Figs. 1k and 1l, the slopes of w_c and $w_c/\widehat{q_{sat}}$ exhibit a clear transition around $\widehat{q_{sat}} = 61$ mm separating tropical convection from events originating from extratropics (indicated by the geographical distribution of $\widehat{q_{sat}}$; low-$\widehat{q_{sat}}$ occurrence mostly along the edge of tropics, sometimes reaching the equator in the central-eastern Pacific; see KSN18, Fig. S13). As $\widehat{q_{sat}}$ exceeds around 61 mm, w_c increases but $w_c/\widehat{q_{sat}}$ decreases; that is, convective onset occurs at higher CWV but at lower column RH. This w_c–$\widehat{q_{sat}}$ relation completely characterizes the

dependence of precipitation pickup on tropospheric temperature in the sense that the conditional precipitation and probability (Figs. 1e,f) collapse well without exhibiting additional temperature dependence. For $\widehat{q_{sat}}$ bins ≥ 70 mm, the PDFs for precipitating events (Fig. 1h) peak right below critical with a common near-Gaussian core; that is, precipitation mostly occurs within a characteristic (and relatively narrow) CWV range around critical. Also, there are more precipitating events below critical for lower $\widehat{q_{sat}}$ (≤ 65.5 mm), consistent with the slightly higher probability in Fig. 1f.

The conditional precipitation and probability in Figs. 1e and 1f are reproduced in Figs. 1i and 1j together with the results from the other tropical ocean basins (20°S–20°N;

colored markers). Here, the statistics from all 4 basins collapse, and are thus indistinguishable. The corresponding values calculated using the PR (2A25) precipitation are also shown (gray dots). Note that Fig. 1j uses a 1.05 mm h^{-1} threshold. The PR and TMI precipitation yield consistent statistics despite that the two instruments slightly differ in sensitivity to low precipitation < 1.05 mm h^{-1}. For $\widehat{q_{\text{sat}}}$ above the transition ($\sim$61 mm), the pickup of conditional precipitation and probability shows little variation across the $\widehat{q_{\text{sat}}}$ range and ocean basins (Figs. 1i,j), and so do the critical values (Figs. 1k,l). For $\widehat{q_{\text{sat}}}$ below the transition, on the other hand, precipitation exhibits a gentler pickup, and the critical values scatter over a wider range. Although not shown here, the qualitative features of the CWV PDFs (for all events and precipitating events) for WPac noted above also apply to other ocean basins.

It is worth noting that the CWV PDFs vary considerably across basins and seasons (not shown), reflecting differences in the CWV–$\widehat{q_{\text{sat}}}$ climatology. However, there is not a clear interannual variability (e.g., ENSO vs non-ENSO years). The conditional precipitation, probability, and the critical values, on the other hand, are robust and exhibit little variation.

We caution the readers to interpret Fig. 1 carefully, especially for results at the highest CWV. The TMIv7.1 CWV retrievals are capped at 75 mm and often contain missing values in the presence of heavy precipitation ($P > 2$ mm h^{-1}). Here, we adopt the gap-filling method tested in KSN18 prior to compiling the statistics. The gap filling partially restores the missing information but inevitably leads to uncertainty, for example, in the distribution of CWV above critical for highest-$\widehat{q_{\text{sat}}}$ bins.

The tropical ARM site data had also been examined to quantify the dependence of convective transition on temporal averaging (not shown). Based on the analysis of satellite retrievals and ground-based measurements in KSN18, the conditional probability of precipitation defined through a reasonable threshold (e.g., $P > 0.25$ mm h^{-1}) would shift toward lower CWV for 1) lower spatial resolution, 2) longer temporal averaging, or 3) lower precipitation threshold, with the shift being less than 10 mm for spatial resolution changing from 0.25° to 2° and/or temporal resolution from snapshot to 6-hourly averaging. This dependence on resolution would not hold for an extreme precipitation threshold (e.g., $P > 10$ mm h^{-1}). In contrast, the conditional precipitation and CWV PDF are insensitive to spatial averaging and less sensitive to temporal averaging.

For more information regarding observed convective transition, see KSN18. Below we summarize key aspects of the basic statistics. In the next section, we will examine the performance of the chosen models with these in mind:

1) The conditional precipitation and probability sharply increase as CWV exceeds the critical CWV w_c.
2) As the bulk tropospheric temperature $\widehat{q_{\text{sat}}}$ increases, w_c increases, but the critical column RH $w_c/\widehat{q_{\text{sat}}}$ decreases.
3) The critical values exhibit little variation across ocean basins.
4) The conditional precipitation and probability can be collapsed by shifting the CWV by w_c.
5) The collapsed conditional precipitation and probability exhibit little variation across the $\widehat{q_{\text{sat}}}$ range and ocean basins.
6) The CWV PDF exhibits a characteristic shape (the low- vs high-CWV peak) that depends on $\widehat{q_{\text{sat}}}$.
7) For CWV above the critical value, the CWV PDF drops rapidly for all $\widehat{q_{\text{sat}}}$. This part of the PDF can be collapsed by shifting the CWV and rescaling the PDF.
8) The PDF of CWV for precipitating events, for the most common $\widehat{q_{\text{sat}}}$ bins over tropical oceans, can be collapsed and shares a common near-Gaussian core.

4. Simulated convective transition statistics in GCMs

a. Convective transition statistics distinguishing convective parameterizations

To assess whether the convective transition statistics can apply as a diagnostic tool targeting convective processes and distinguish the realism of convective parameterizations adopted by models, in this subsection, we examine the basic statistics compiled using the hourly data from two pairs of GCMs. The configurations/models within each pair differ primarily in their representations of moist convection, which is expected to be the key difference for the examined statistics analyzed here.

The first pair of GCMs consists of two $\sim$1° configurations of the latest global model AM4 (Zhao et al. 2018a,b) developed by the GFDL that are equipped with different convective schemes, namely, the AM4G9 with the double-plume convective scheme (Zhao et al. 2009), and the AM4B6 with the Donner convective scheme (Donner 1993).

The second pair is based on the CAM developed by the NCAR, namely, the CAM5.3 ($\sim$1°; Neale et al. 2012) with the default Zhang–McFarlane convective parameterization (Zhang and McFarlane 1995), and the SPCAM ($\sim$2°) with a 2D CRM for simulating moist convection (Khairoutdinov and Randall 2003). Both models share the same dynamic core.
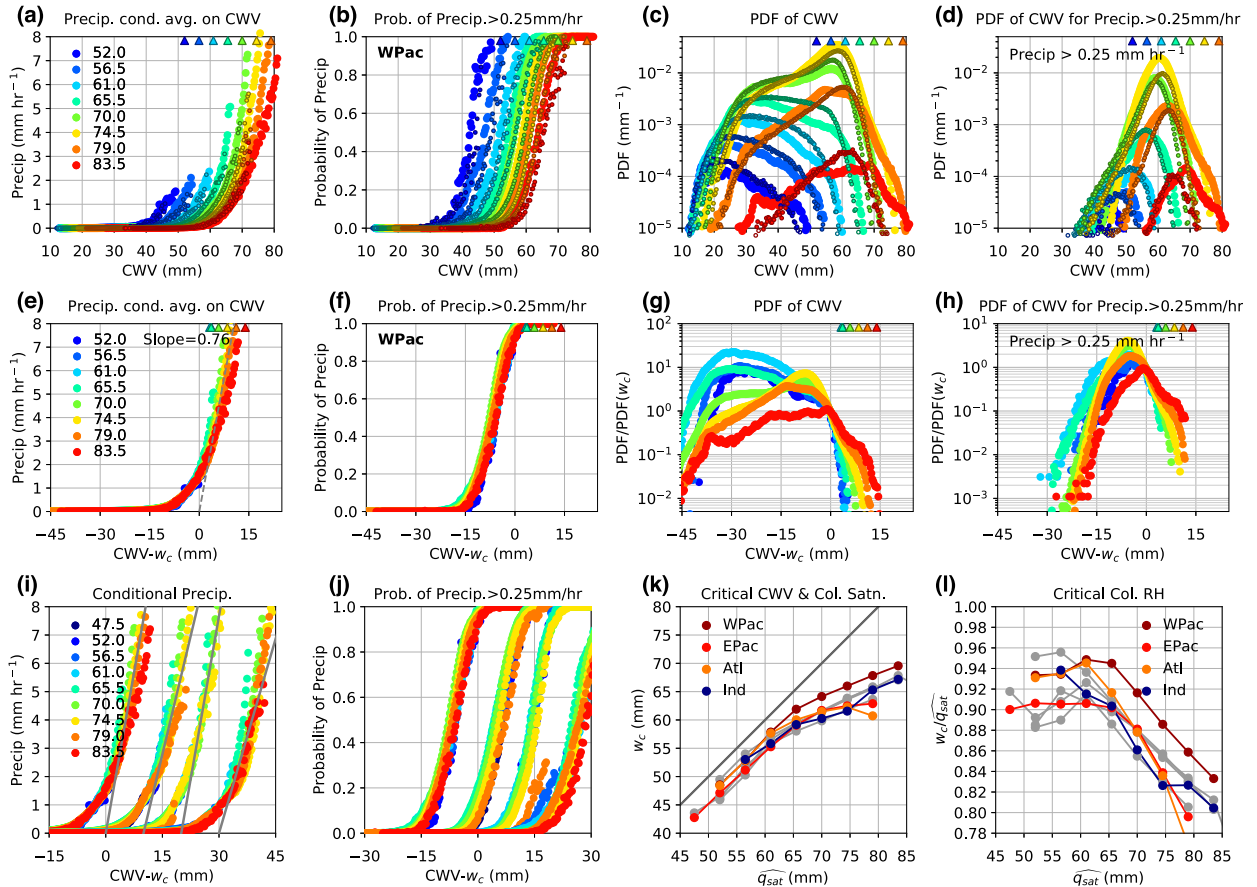
FIG. 2. As in Fig. 1, but compiled using the AM4G9 output (~1°, hourly). Statistics in Figs. 1a–d are reproduced as smaller markers in (a)–(d) here for visual reference, and critical values in Figs. 1k and 1l are reproduced in (k) and (l) as gray makers. In (i) and (j), statistics from the four tropical ocean basins are shifted with 10-mm increments for ease in viewing.

Like the observed statistics in Fig. 1, Figs. 2–5 show the same sets simulated in the models listed above. The observed statistics in Figs. 1a–d are reproduced as small markers for visual reference in Figs. 2a–d; the simulated statistics in Figs. 2i and 2j are shifted for ease in viewing [with 10-mm increments; from left to right: tropical WPac and eastern Pacific (EPac), Atlantic (Atl) and Indian Ocean (Ind)]; the observed critical values in Figs. 1k and 1l are reproduced in gray in Figs. 2k and 2l and the same for the corresponding panels in Figs. 3–5. We note in Fig. 5 (SPCAM), because of lower precipitation rates, the range of the linear fit in Figs. 5e and 5i had to be reduced to 1.5–2.5 mm h^{-1} (as opposed to 3–5 mm h^{-1} for observations and other models).

All four models capture the observed pickup of precipitation and probability; they also capture the observed dependence of the critical CWV and critical column RH as a function of $\widehat{q_{sat}}$ (Figs. 2–5k,l). However, the simulated conditional probability (Figs. 2–5b,f,j) shows departures from observations to varying extents, reflecting the disagreement in the joint

distribution of CWV and precipitation rate P (discussed later in section 5). The collapsed version of the simulated statistics in Figs. 2e–j, 3e–j, 4e–j, and 5e–j also demonstrate that the w_c–$\widehat{q_{sat}}$ relation does not completely characterize the temperature dependence in these models, for example, the slope of the best fit to the conditional precipitation and the conditional probability show sensitivity to $\widehat{q_{sat}}$ (Figs. 2–5e,f,i,j); Additionally, the CWV PDFs for high $\widehat{q_{sat}}$ do not drop rapidly around critical (Figs. 2–5g,h), that is, more above-critical events than observed, indicating a tendency of excessive moisture convergence or surface evaporation during precipitation in models. The following sections examine each model in greater detail.

1) AM4G9 (DOUBLE-PLUME CONVECTIVE SCHEME)

According to Fig. 2, the simulated conditional precipitation by AM4G9 quantitatively agrees with observations (Fig. 2a), with the slope of the best fit being slightly higher than observed (Fig. 2e vs Fig. 1e) but still
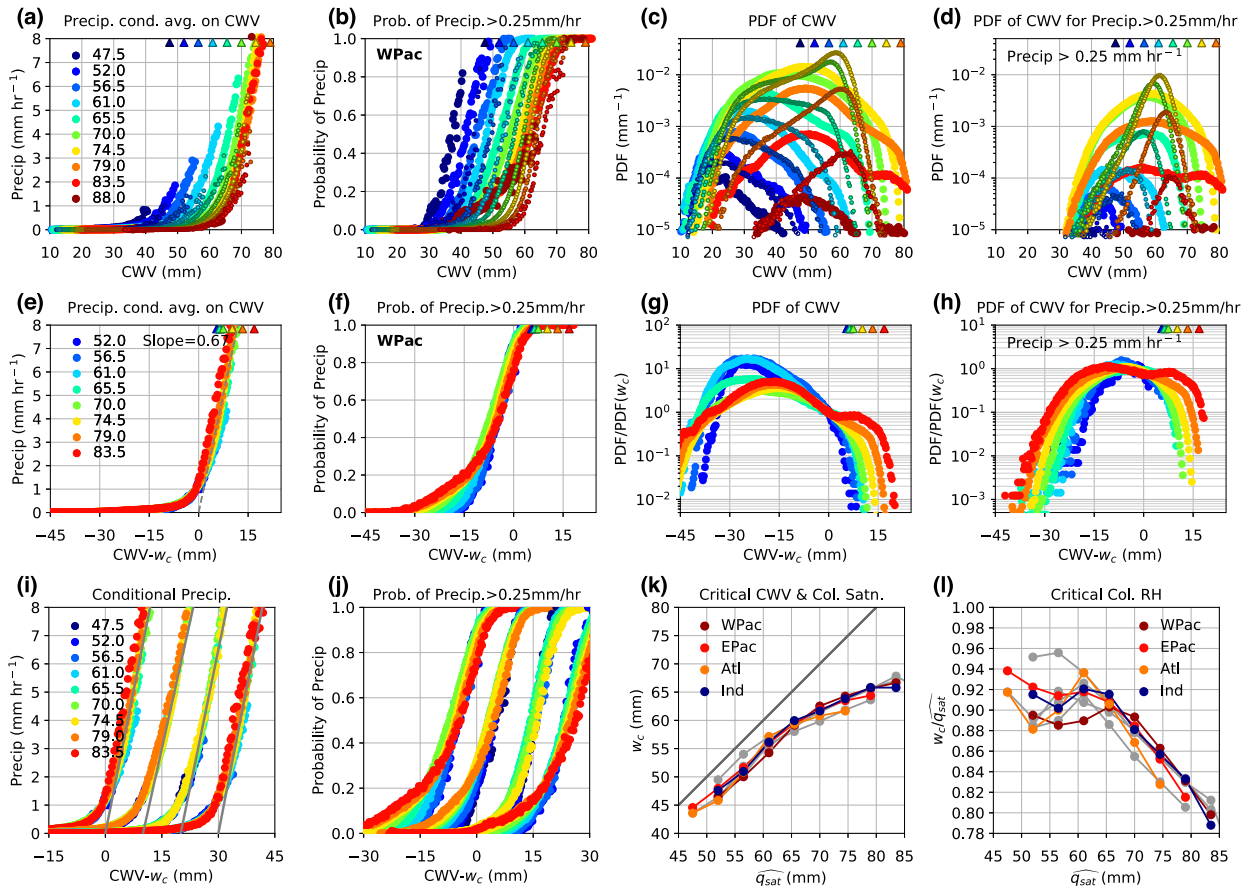
FIG. 3. As in Fig. 2, but compiled using the AM4B6 output (~1°, hourly).

within the range of observational uncertainty (e.g., caused by CWV gap filling). The slope also modestly varies with $\widehat{q_{\text{sat}}}$ (Fig. 2e) and across ocean basins (Fig. 2i). The simulated conditional probability has a steeper pickup occurring at slightly lower CWV (Fig. 2b). The simulated CWV PDF (Fig. 2c), that is, the joint PDF of CWV and $\widehat{q_{\text{sat}}}$, matches observations but also exhibits modestly more above-critical events for highest $\widehat{q_{\text{sat}}}$ bins (Fig. 2g). However, given the uncertainty in the CWV retrievals at high values, it is inconclusive at this time whether this mismatch in the PDF implies the model misbehaving. The simulated PDF for precipitating events shows that there are more below-critical precipitating events for low $\widehat{q_{\text{sat}}}$, resembling observations (Figs. 2h and 1h). The simulated critical values (Figs. 2k,l) exhibit a clear transition around $\widehat{q_{\text{sat}}} = 61$ mm and are consistent with observations, with slightly higher values for WPac.

2) AM4B6 (DONNER CONVECTIVE SCHEME)

In Fig. 3, the simulated conditional precipitation by AM4B6 roughly matches observations for $\widehat{q_{\text{sat}}}$

bins ≥ 70 mm (Fig. 3a), with the best-fit slope slightly increasing with $\widehat{q_{\text{sat}}}$ (Fig. 3e). The simulated critical values (Figs. 3k,l) agree with observations and display a transition around $\widehat{q_{\text{sat}}} = 61$ mm. However, discrepancies exist in the simulated conditional probability and CWV PDFs. The collapsed conditional precipitation shows little variation across basins (Fig. 3i), but its pickup is gentler than observed (Fig. 3b) and exhibits dependence on $\widehat{q_{\text{sat}}}$ for CWV below critical (Fig. 3f); that is, there are more below-critical precipitating events for high $\widehat{q_{\text{sat}}}$ compared to observations (Fig. 3h vs Fig. 1h). While the characteristic shape of the simulated PDFs of CWV (Fig. 3c) for low-$\widehat{q_{\text{sat}}}$ bins is consistent with observations, the high-CWV peak around critical fails to develop as $\widehat{q_{\text{sat}}}$ increases. Furthermore, the simulated CWV PDF extends into the above-critical range for highest-$\widehat{q_{\text{sat}}}$ bins (Fig. 3g), implying the moisture convergence in warm, moist environments is stronger than suggested by observations.

An additional set of output from the 0.5° version of AM4B6 has also been analyzed, and the resulting statistics closely resemble those for 1° shown in Fig. 3,
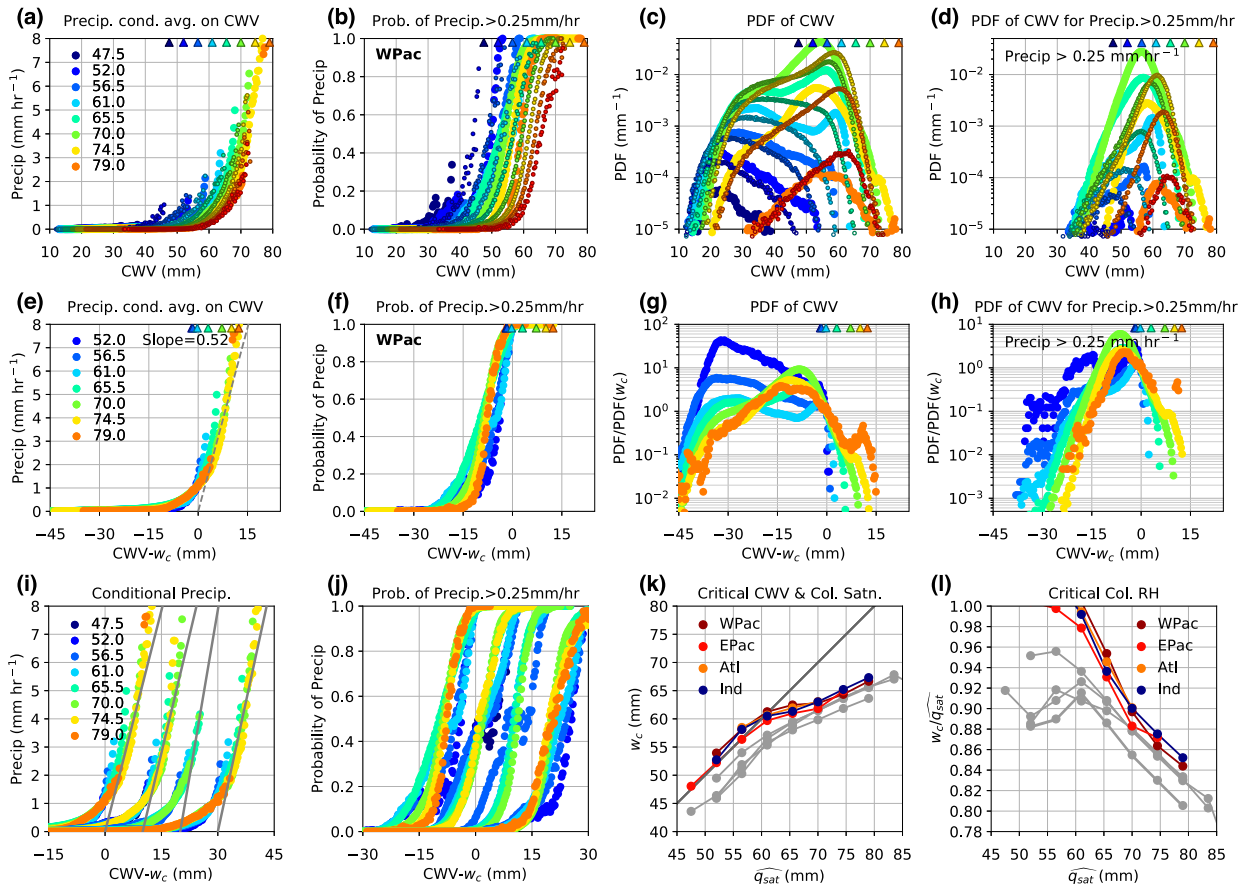
FIG. 4. As in Fig. 2, but compiled using the CAM5.3 output (~1°, hourly).

with minor quantitative differences (not shown). This is indicative that comparing models of different resolution may still be relevant for diagnosis of convective transition.

3) CAM5.3 (ZHANG–MCFARLANE CONVECTIVE SCHEME)

In Fig. 4, the simulated conditional precipitation by this version of CAM5.3 picks up at higher CWV than observed (Fig. 4a), resulting in higher critical values (especially for lower-$\widehat{q_{sat}}$ bins; Figs. 4k and 4l). The best-fit slope is slightly lower than observed (but still within the observational uncertainty) and exhibits weak dependence on $\widehat{q_{sat}}$ (Fig. 4e) with modest variation across basins (Fig. 4i). On the other hand, the simulated conditional probability picks up at lower CWV (Fig. 4b; $P > 0.25\,\mathrm{mm\,h^{-1}}$). The collapsed conditional probability also exhibits dependence on $\widehat{q_{sat}}$ with slightly steeper pickup for higher $\widehat{q_{sat}}$ (Fig. 4f), and exhibits noticeable irregularities, that is, non-monotonic in CWV for $\widehat{q_{sat}} = 47.5\,\mathrm{mm}$ in EPac and for $\widehat{q_{sat}} = 56.5\,\mathrm{mm}$ in Atl (Fig. 4j). The simulated CWV

PDFs (Fig. 4c) reveal a cold bias in the model with 70 mm instead of 74.5 mm being the most probable $\widehat{q_{sat}}$ for WPac, and this cold bias also appears in other tropical ocean basins. The characteristic shape of the PDFs generally agrees with observations (Fig. 4c), but also exhibits more above-critical events for highest-$\widehat{q_{sat}}$ bins, subject to the uncertainty of the CWV retrievals at high values (Fig. 4g; like Fig. 2g for AM4G9). In Fig. 4c, the CWV PDF for $\widehat{q_{sat}} = 61\,\mathrm{mm}$ has two peaks, implying a bimodal distribution of SST (Neelin et al. 2009) instead of a smoother transition from cold to warm SST (or low-level divergence to convergence) suggested by observations.

4) SPCAM (SUPERPARAMETERIZATION USING A 2D CLOUD-RESOLVING MODEL)

In Fig. 5, the simulated precipitation–CWV relationship by SPCAM is decent despite the lower resolution (~2°) for the host GCM grid [note the grid spacing of the 2D cloud-resolving model (CRM) is 4 km]. The pickup of the simulated conditional precipitation and probability is less steep compared with
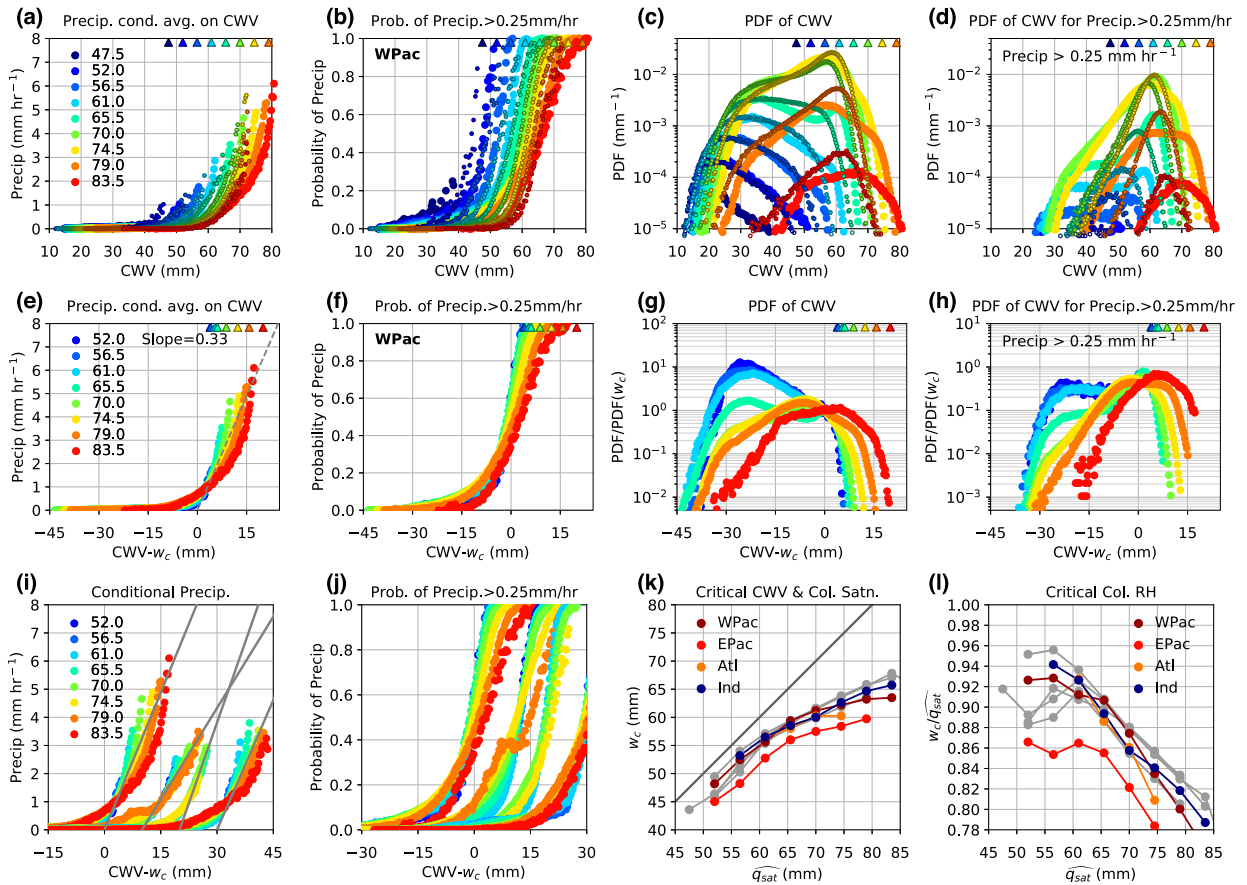
FIG. 5. As in Fig. 2, but compiled using the SPCAM output ($\sim 2°$, hourly). In (k) and (l), the values of w_c are calculated by fitting the conditionally averaged precipitation rate in the range 1.5–2.5 mm h^{-1}.

observations (Figs. 5a,b) and exhibits a $\widehat{q_{sat}}$ dependence with gentler pickup for higher $\widehat{q_{sat}}$ (Figs. 5e,f). Note that in Fig. 5b, as CWV increases from below critical, the simulated conditional probability for $\widehat{q_{sat}}$ bins ≤ 74.5 mm increases roughly linearly until reaching a probability of ~ 0.15, and then sharply increases with further CWV increment, exhibiting a two-step pickup. The pickup also displays a great variation across basins (Figs. 5i,j), and irregular behavior of the simulated conditional probability can be noted for $\widehat{q_{sat}} = 79$ mm in EPac. On the other hand, the simulated critical values generally agree with observations, with lower values for EPac (Figs. 5k,l). For low-$\widehat{q_{sat}}$ bins (≤ 61 mm), the simulated CWV PDFs are consistent with observations (Fig. 5c), with a bimodal PDF for $\widehat{q_{sat}} = 65.5$ mm (like Fig. 4c, 61-mm bin). For even higher-$\widehat{q_{sat}}$ bins, the high-CWV peak around critical is less distinctive compared to observations, and the PDF also extends into the above-critical regime (like Fig. 3g for AM4B6).

The statistics presented in Fig. 5 are from an SPCAM simulation with prescribed SST. Another SPCAM run

coupled with a slab ocean model (SOM; Bitz et al. 2012) leads to similar statistics with a slightly shifted joint PDF of CWV and $\widehat{q_{sat}}$, reflecting changes in the mean climate state (not shown). This is indicative that coupling with different model components (e.g., ocean model) does not alter the simulated convective transition, which primarily depends on the representation of convective physics. This is also supported by a set of CNRM simulations discussed later in section 4b(3). Also note that the statistics exhibit little sensitivity to doubling the CRM domain size (4 km $\times$ 64 columns vs 32 columns) to permit more organized convective events (not shown).

b. Convective transition in MJOTF/GASS models

The last subsection has demonstrated that hourly model data is suitable for the diagnosis of fast-time-scale convective transition. However, most high-frequency output from the recent CMIP5 are daily or 6 hourly, and higher frequencies are uncommon. To establish that 6-hourly data can also be useful for diagnosing convective transition, and to survey the performance
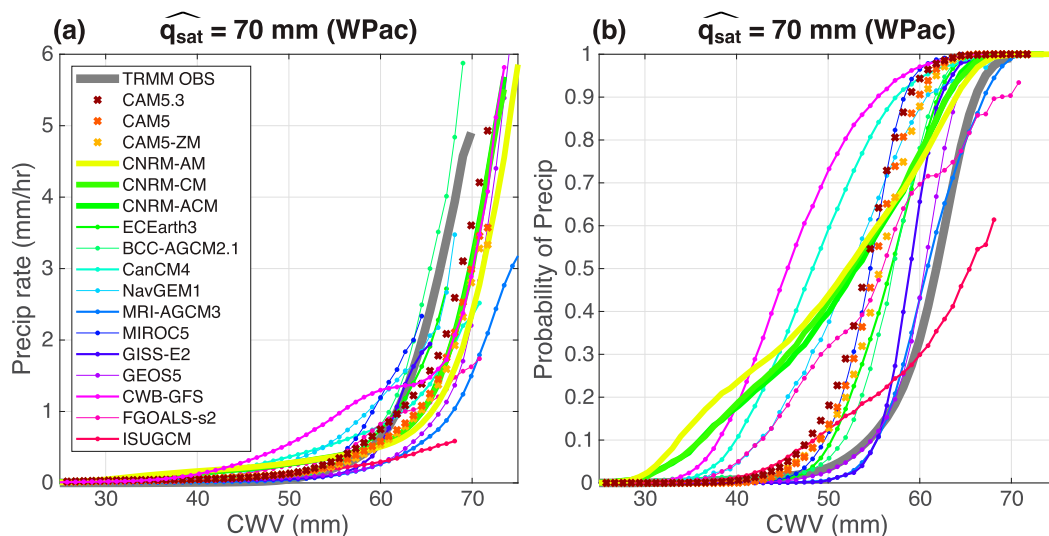
FIG. 6. (a) Conditionally averaged precipitation rate for $\widehat{q_{sat}}$ = 70 mm in the tropical WPac sampled from the MJOTF/GASS ensemble. (b) As in (a), but for conditional probability of precipitation ($P > 0.25$ mm h^{-1}). Here, the TRMM OBS is reproduced from Figs. 1a and 1b, and CAM5.3 is reproduced from Figs. 4a and 4b for visual reference. The MJOTF/GASS model data are 6 hourly (average for precipitation) and had been regridded to 2.5° resolution prior to our analysis. See Fig. S1 for MJOTF/GASS ensemble statistics for other $\widehat{q_{sat}}$ bins.

of current mainstream GCMs, in this subsection we sample the basic statistics for particular $\widehat{q_{sat}}$ bins using the 6-hourly output (snapshot for CWV and $\widehat{q_{sat}}$, average for precipitation; regridded to 2.5° × 2.5° resolution) from a subset of models (simulations 5–20 in Table 1) from the MJOTF/GASS project.

Figure 6 shows the conditional precipitation and probability of precipitation ($P > 0.25$ mm h^{-1}) for the 70-mm $\widehat{q_{sat}}$ bin for WPac sampled from the MJOTF/GASS models, together with observations (TRMM OBS; as in Fig. 1) and hourly 1°CAM5.3 (as in Fig. 4). The corresponding CWV PDFs are presented in Figs. 7a–c for different $\widehat{q_{sat}}$ bins from low to high relative to the most probable $\widehat{q_{sat}}$ in each case (bins chosen to contrast differences). A single $\widehat{q_{sat}}$ is sufficient to demonstrate the typical behavior for the precipitation pickup, while three $\widehat{q_{sat}}$ values illustrate the typical behavior of the PDFs. For the complete set of statistics for the MJOTF/GASS models, see Fig. S1 in the online supplemental material.

1) GENERAL OVERVIEW

Figure 6a displays considerable variation across models. Most models produce a qualitatively reasonable pickup of precipitation above some threshold in CWV, but the exact value varies considerably. Qualitative departures from the observed behavior can be noted for some models. For instance, CWB-GFS and FGOALS-s2 exhibit a two-step pickup, and precipitation in the ISUGCM is relatively insensitive to CWV. The pickup

of precipitation in many models occurs at higher CWV compared to observations. In contrast, the simulated conditional probability (Fig. 6b) in most models sharply increases at CWV much lower than observed, and this departure from observations is too large to be explained by the dependence of conditional probability on spatial and time averaging (1° snapshot for observations vs 2.5° 6-hourly average for MJOTF/GASS models). Following section 3, the estimated shift caused by averaging is on the order of 5–10 mm or smaller compared to the shifts of up to 20 mm exhibited here. The low conditional precipitation and high conditional probability (for $P > 0.25$ mm h^{-1}; well above detection limit of the TMI and PR; TRMM 2011; Wentz et al. 2015) at CWV below critical in these models imply a widespread problem with excessive occurrence of low rain rates—which for brevity we refer to as a drizzle problem at subdaily time scales (not to be confused with the conventional drizzle problem for daily mean; e.g., Dai 2006).

Turning to the CWV PDF, as noted in section 3 (Fig. 1c), at low $\widehat{q_{sat}}$, the PDF peaks at low CWV below which the PDF drops sharply, and above which the PDF decreases slowly. As $\widehat{q_{sat}}$ increases, another peak develops at high CWV around critical with the low-CWV peak diminishing. In Fig. 7a, the simulated PDFs for low $\widehat{q_{sat}}$ by all models qualitatively resemble the observed low-CWV peak. But the transition to high-CWV peak as $\widehat{q_{sat}}$ increases (Figs. 7b,c) is correctly captured only by some of the models (e.g., CAM5 cases, MRI-AGCM3,
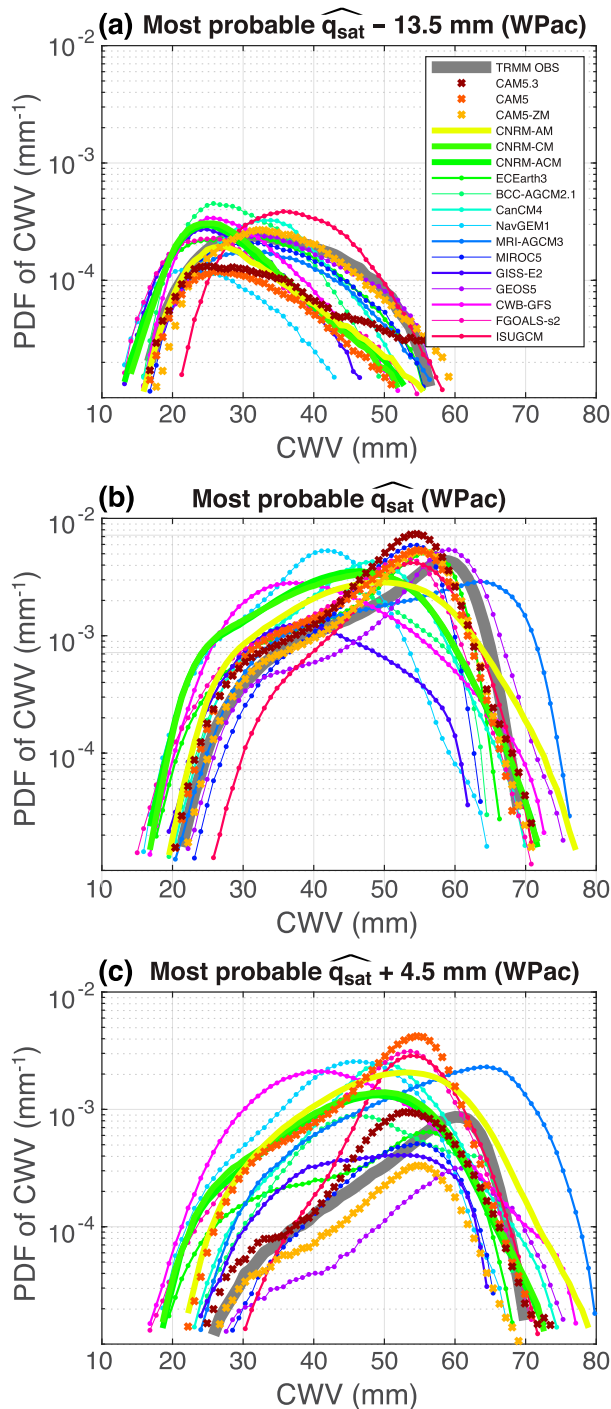
(a) Most probable $\widehat{q_{sat}}$ − 13.5 mm (WPac)

Legend:
- TRMM OBS
- CAM5.3
- CAM5
- CAM5-ZM
- CNRM-AM
- CNRM-CM
- CNRM-ACM
- ECEarth3
- BCC-AGCM2.1
- CanCM4
- NavGEM1
- MRI-AGCM3
- MIROC5
- GISS-E2
- GEOS5
- CWB-GFS
- FGOALS-s2
- ISUGCM

(b) Most probable $\widehat{q_{sat}}$ (WPac)

(c) Most probable $\widehat{q_{sat}}$ + 4.5 mm (WPac)

FIG. 7. (a) PDFs of CWV for the most probable $\widehat{q_{sat}}$ − 13.5 mm (i.e., a relatively cold bin) in the tropical WPac sampled from the MJOTF/GASS ensemble. (b) As in (a), but for the most probable $\widehat{q_{sat}}$ bin. (c) As in (a), but for the most probable $\widehat{q_{sat}}$ + 4.5 mm (i.e., a relatively warm bin). Here, the most probable $\widehat{q_{sat}}$ value is found separately for each case. The TRMM OBS is reproduced from Fig. 1c, and CAM5.3 is reproduced from Figs. 4c for visual reference. See Fig. S1 for MJOTF/GASS ensemble statistics for other $\widehat{q_{sat}}$ bins.

and GEOS-5). In the other models, the high-CWV peak has a wider spread (CanCM4, NavGEM1, and CNRM cases) or fails to develop (CWB-GFS). Note that whether a model can capture this transition of PDF at high $\widehat{q_{sat}}$ is in part related to its ability to simulate precipitation pickup, with models that have a less sharp pickup tending to have PDFs that have insufficiently sharp peaks for the most common $\widehat{q_{sat}}$. However, this relationship is not perfect; for instance, ISUGCM has a very slow pickup, but while the pickup peak occurs at too-low CWV, the excessive breadth of its PDF is not as bad as might be anticipated from its simulation of the pickup.

Next, we concentrate on two subsets of models for which we have multiple instances: the CAM5 and CNRM.

2) CAM5 COMPARISONS

There are three CAM5 instances (represented by crosses in Figs. 6 and 7): CAM5.3, CAM5, and CAM5-ZM. CAM5.3 and CAM5 primarily differ in spatial (1° vs 2.5°; originally simulated at the same resolution) and temporal resolution (hourly vs 6-hourly average), which presumably lead to the minor differences in Fig. 6 (a small shift in CWV) and PDFs in Fig. 7. However, the precipitation pickup in CAM5.3 and CAM5 closely resemble each other (see also Fig. S1), which is consistent with the insensitivity to spatial and time averaging noted in observations (section 3; KSN18). This demonstrates that conventional 6-hourly model data are useful for fast-time-scale convective transition diagnosis, thus extending the applicability of such metrics.

For CAM5 versus CAM5-ZM, the latter configuration adopted a modified Zhang–McFarlane deep convective parameterization with a new microphysics scheme for convective clouds (Song and Zhang 2011). Nevertheless, the resulting statistics in Figs. 6 and 7 are very similar, suggesting that the formulation of entraining plume and mass flux closure are more important than microphysics to the convective transition (see Fig. S1; small differences between the two most probable $\widehat{q_{sat}}$ bins in the CAM5 and CAM5-ZM lead to apparent differences in the magnitude of the peak in Fig. 7, while the shapes are similar). Whether this will hold for other models requires further investigation.

3) CNRM COMPARISONS

There are three CNRM instances (thick solid lines in Figs. 6 and 7): CNRM-AM, CNRM-CM, and CNRM-ACM. Here the suffixes AM and CM stand for atmosphere-only and coupled simulations, and ACM for atmosphere-only run forced by the monthly mean

SST and sea ice output from the coupled simulation (Jiang et al. 2015). That is, they differ in coupling or forcing through lower boundary.

CNRM-CM and CNRM-ACM produce almost identical statistics in Figs. 6 and 7. The uncoupled version, CNRM-AM, quantitatively differ in CWV PDF from the other two, tending to be shifted toward higher values in Fig. 7. However, the pickup of precipitation (Fig. 6) and qualitative features of the CWV PDF (Fig. 7 and Fig. S1) are alike for all 3 cases, and the most common $\widehat{q_{sat}}$ value, 65.5 versus 70 mm, indicates that the coupled/forced versions are residing overall at lower temperatures. These differences are consistent with the fast-time-scale convective transition operating similarly among these versions, as in the SPCAM comparisons [section 4a(4)], while the overall effects of the coupling and forcing through lower boundary affect the probability distribution of temperature and water vapor, associated with differences in climatology.

c. Summary of model behavior

Sections 4a and 4b are suggestive that the basic statistics can distinguish convective parameterizations and are less sensitive to other model components, for example, cloud microphysics, coupling, and forcing configurations. Furthermore, the qualitative features of the basic statistics are reasonably robust to spatial and time averaging, making it possible to leverage the existing CMIP effort for such fast-time-scale diagnosis. Across the tested models there is great variation in various aspects, which must be examined separately to comprehensively assess parameterization schemes.

The observed precipitation–CWV relationship has been attributed to the impact of tropospheric moisture on conditional instability through entrainment (Holloway and Neelin 2009; Schiro et al. 2016; Kuo et al. 2017). The exact functional forms of simulated conditional precipitation and probability vary considerably, but all models capable of simulating precipitation pickup can reproduce the dependence of critical CWV w_c and critical column RH $w_c/\widehat{q_{sat}}$ on $\widehat{q_{sat}}$ (including those from the MJOTF/GASS project; not shown), although quantitative differences are noted in the values of w_c. This could be consistent with the observed w_c–$\widehat{q_{sat}}$ relation arising from entrainment, as demonstrated by offline entraining plume calculations (Sahany et al. 2012) and perturbed physics experiments (Kuo et al. 2017), since the models differ in their entrainment representations. However, we cannot exclude other intermodel differences as potentially contributing to this spread.

The conditional probability in most models picks up at below-critical CWV lower than observed, which cannot be fully explained by the difference in spatial and time averaging of the data, revealing a widespread drizzle problem at subdaily/hourly time scales. The traditional use of the term ''drizzle problem'' concerns excessive occurrence of low daily mean intensities (Dai 2006) without specifying the underlying thermodynamic environment. Here, conditioned on the bulk parameters (CWV, $\widehat{q_{sat}}$) that tend to vary slowly compared with subdaily/hourly time scales, the statistics indicate misrepresented precipitation processes in many of the models.

In the model for which we have a direct comparison of different microphysics schemes (CAM5.3 vs CAM5-ZM), only very small impact on the drizzle problem was noted. On the other hand, perturbed physics experiments (Kuo et al. 2017) indicate that the entrainment value can strongly affect this issue, since low entrainment yields insufficient dependence on free-tropospheric moisture and thus overly frequent occurrence of rainfall. Analysis of such perturbed physics experiments across a wide set of convective parameters, combined with conceptual modeling, would be useful to further understand such intermodel differences.

Some of the models qualitatively capture the form of the PDFs of CWV and the dependence of these on temperature seen in observations, but many do poorly in this comparison. The PDF in the dry (nonprecipitating) regime is expected to be influenced by dynamics other than the convective physics alone. The PDFs at colder temperatures, which reflect more of the dry regime, tend to be better simulated than the high-temperature, high-CWV range that has stronger dependence on the convective physics. Comparison of models with coupled versus uncoupled versions and different coupling/forcing settings through lower boundary (SPCAM and CNRM cases) indicates that the shapes of the PDFs tend to be similar, but shifts in climatology are reflected in the probability distribution of temperatures and water vapor.

Note that small errors in the onset of precipitation could have significant implications. For instance, the values of critical CWV determine the CWV PDF peak locations in observations and some of the models. Thus, a bias of a few millimeters in the critical values, compared with the observed climatological mean of ∼41 mm over tropical oceans, and more generally, biases in the CWV PDFs, could substantially alter the longwave radiation budget.

Overall the spread among the models and departures from observations in these fast-process diagnostics to which they have not previously been compared is of considerable concern for model development. But the existence of some models that do well at these diagnostics is encouraging.

5. Joint probability distributions of precipitation and CWV

In this section, we further examine the joint PDF of precipitation rate P and CWV (relative to critical, $CWV - w_c$) compiled from observations and hourly data of the AM4G9, AM4B6, CAM5.3, and SPCAM. Recall that the former two AM4 instances adopt different convective parameterizations, and the latter two are CAM cases sharing the same dynamic components but differing in moist convective representations (parameterizations vs 2D CRM).

To help interpret the joint PDF, consider the decomposition:

$$\text{Prob}(P, CWV - w_c) = \text{Prob}(P|CWV - w_c) \\ \times \text{Prob}(CWV - w_c),$$

where the three Prob terms from left to right represent, respectively, the joint PDF of P and $CWV - w_c$, the conditional probability distribution of P given $CWV - w_c$, and the PDF of $CWV - w_c$. Each of these quantities potentially depends also on bulk tropospheric temperature $\widehat{q_{sat}}$ and ocean basin, but these are omitted from the notation for simplicity. $\text{Prob}(P|CWV - w_c)$ characterizes the probability distribution of precipitation for a given large-scale temperature–moisture environment (with temperature entering via w_c). $\text{Prob}(CWV - w_c)$ reflects the interaction of the large-scale environment with convective physics (to the extent this environment is captured by CWV and $\widehat{q_{sat}}$). Note that even if a model permits an accurate estimate of precipitation given a large-scale temperature–moisture environment [e.g., with a correct $\text{Prob}(P|CWV - w_c)$], the joint PDF would still be affected by $\text{Prob}(CWV - w_c)$, which is expected to be more vulnerable to large-scale flow interacting with convective physics and subsequent feedbacks.

Below, we first examine the joint PDFs in Fig. 8, and then Figs. 9 and 10 for a quantitative breakdown of these distributions.

a. Joint PDF of precipitation and CWV relative to critical

Figure 8a (color shading) shows the joint PDF of P and $CWV - w_c$ for the most probable $\widehat{q_{sat}}$ bin (74.5 mm) in the tropical WPac compiled at 1° using the PR precipitation, TMIv7.1 CWV and Reanalysis-2 temperature. Here, the color increments correspond to a doubling of the PDF value. The "nonprecipitating" bins ($0 \leq P \leq 0.05 \text{ mm h}^{-1}$) are enlarged in the vertical along the bottom for visual clarity, and the orange dotted lines represent the conditional probability of $P > 0.05 \text{ mm h}^{-1}$,

providing an alternate display of the ratio of the nonprecipitating bins. The gray shading indicates CWV > 75 mm at which the TMIv7.1 CWV is capped. The corresponding conditional mean (blue solid), variance (blue dashed), and median (magenta solid) of precipitation are also shown for reference. The same set of statistics compiled using the TMIv7.1 precipitation is displayed in Fig. 8b, and those simulated by models in Figs. 8c–f. Compared to PR, the TMIv7.1 precipitation has a spurious cutoff around $P \sim 10 \text{ mm h}^{-1}$ (presumably retrieval dependent; see Fig. 9b vs Fig. 9a) but contains more events than the PR when coarse grained to 1°. Hence both are included in Fig. 8.

In Fig. 8a, an abrupt transition from the dry to moist regime occurs around $CWV - w_c \sim -10 \text{ mm}$ below which only weak precipitation is permitted, and above which strong precipitation becomes frequent. However, this transition occurs considerably lower than critical, implying that the rapid increase of the conditional precipitation (blue solid) near critical is partly contributed by the decreasing ratio of nonprecipitating versus precipitating events as CWV increases and exceeds critical. This is also reflected by the pickup of conditional probability (orange dotted) and median (magenta solid) around the same location. One can contrast the conditional precipitation that sharply increases with the more detailed behavior of the joint PDF. From slightly below critical to slightly above critical, a roughly exponential tail toward high precipitation values may be seen, and the properties of this tail do not change dramatically as a function of CWV in this range (see also Fig. 9a). The joint PDF exhibits the highest probability of high precipitation near critical, partly because the CWV PDF peaks around critical. The statistics in Fig. 8b generally agree with those in Fig. 8a (differences may be noted later in Fig. 9b vs Fib. 9a).

The model-simulated joint PDFs in Figs. 8c–f qualitatively capture many features of the observations, but the dry-to-moist transition is less drastic than observed. Another notable difference seen to some extent in all models is in the behavior of the tail of the PDF extending to high precipitation as a function of CWV. The tail tends to extend further toward strong precipitation as CWV increases above critical ($CWV - w_c > 5 \text{ mm}$), indicating departures from observations in $\text{Prob}(P|CWV - w_c)$ and/or $\text{Prob}(CWV - w_c)$. One can also see the conditional precipitation tending to coincide more closely with the conditional median in the models, implying a relatively symmetric P distribution at odds with the observed asymmetry. Variations among the models in these differences relative to observations may be noted: AM4G9 and SPCAM can produce strong precipitation for CWV around or right below critical, while AM4B6
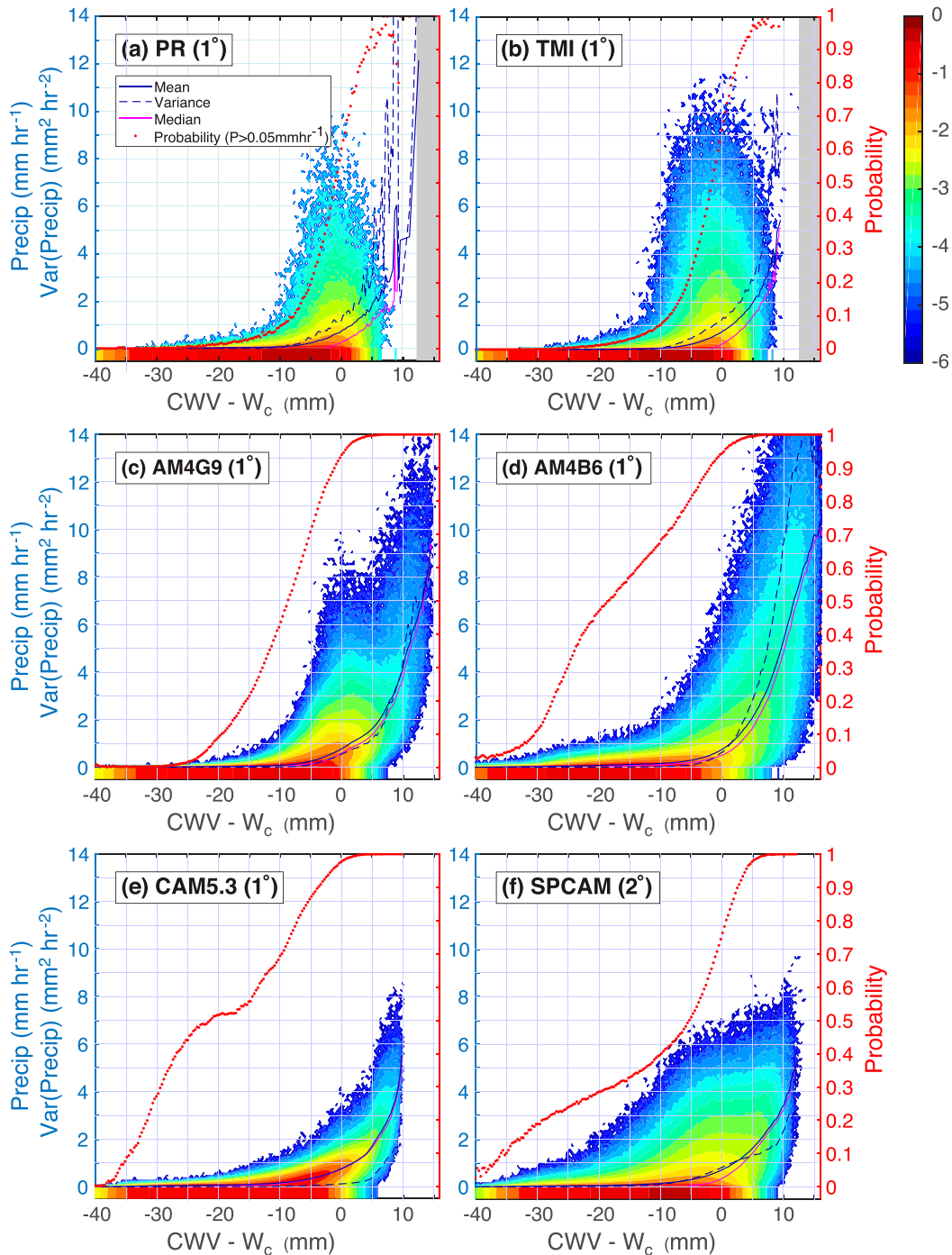
FIG. 8. (a) Joint PDF (color shading; mm^{-2} h), on a $\log_{10}$ scale, of CWV relative to critical and precipitation rate P for the 74.5-mm $\widehat{q_{sat}}$ bin in the tropical western Pacific compiled at 1° using the PR 2A25 precipitation rate, TMIv7.1 CWV, and Reanalysis-2 temperature. The color increments correspond to a doubling of the PDF value (note that $10^{0.3} \approx 2$). The "nonprecipitating" bins ($0 \leq P \leq 0.05$ mm h^{-1}) are enlarged in the vertical along the bottom for visual clarity. The conditional mean (solid blue), median (solid magenta), variance (dashed blue), and probability of precipitation ($P > 0.05$ mm h^{-1}; orange dots), all as a function of CWV, are also displayed for reference (note separate y axes for precipitation and probability; variance is on the same axis as precipitation, but in different units). (b) As in (a), but with the PR 2A25 precipitation rate replaced by TMIv7.1 precipitation rate. (c)–(f) As in (a), but compiled using the hourly output from AM4G9, AM4B6, CAM5.3, and SPCAM, respectively. In (a) and (b), the gray shading represent where the TMIv7.1 CWV value is capped at 75 mm and is hence unavailable.
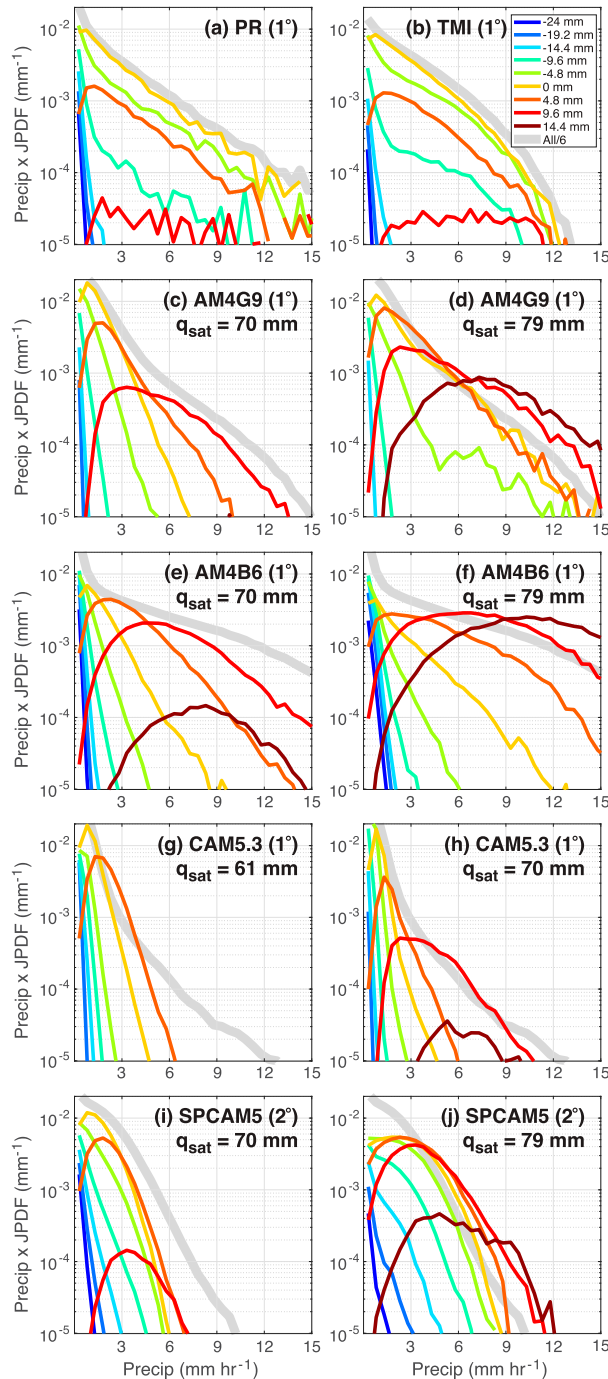
FIG. 9. (a) The precipitation contribution (i.e., precipitation-rate-weighted joint PDF), as a function of precipitation rate P and CWV relative to critical (colors), for the 74.5-mm $\widehat{q_{\mathrm{sat}}}$ bin in the tropical WPac compiled at 1° using the PR 2A25 precipitation rate, TMIv7.1 CWV, and Reanalysis-2 temperature. Here, the calculation uses the joint PDF displayed in Fig. 8a. The gray line represent the overall (i.e., including all CWV and $\widehat{q_{\mathrm{sat}}}$) precipitation contribution for WPac (dimensionless) shifted downward by a factor of 6 for visual reference. (b) As in (a), but with the PR 2A25 precipitation rate replaced by TMIv7.1 precipitation rate. (c),(d) As in (a), but for a relatively cold $\widehat{q_{\mathrm{sat}}}$ bin and a relatively warm $\widehat{q_{\mathrm{sat}}}$ bin, respectively,

and CAM5.3 cannot. All 4 models underestimate the conditional P variance, but CAM5.3 is the most serious one.

KSN18 has noted that the observed joint PDF shows little variation across the $\widehat{q_{\mathrm{sat}}}$ range and ocean basins (except the ratio of precipitating vs nonprecipitating events for below-critical CWV may vary significantly). That is, the value of CWV $- w_c$ alone characterizes the probability distribution of precipitation in the moist regime, and this precipitation–CWV relation does not exhibit additional dependence on $\widehat{q_{\mathrm{sat}}}$. As such, only the results for the most probable $\widehat{q_{\mathrm{sat}}}$ are displayed in Figs. 8a and 8b (and the qualitative characteristics noted in Figs. 8c–f are generally valid). However, the model-simulated distributions exhibit spurious dependence on $\widehat{q_{\mathrm{sat}}}$, as shown in Fig. 9.

b. Precipitation contributions

Figures 9a and 9b show the amount of total rainfall accumulation contributed by each P intensity, or precipitation contribution (i.e., P-weighted joint PDF), for various values of CWV $- w_c$ (colors) calculated using the same joint PDFs in Figs. 8a and 8b, with different bin width. The gray lines represent the overall (i.e., including all CWV and $\widehat{q_{\mathrm{sat}}}$) precipitation contribution for WPac (dimensionless; shifted downward by a factor of 6 for visual reference). The corresponding results simulated by models are in Figs. 9c–j, with panels on the left displaying a low-$\widehat{q_{\mathrm{sat}}}$ bin (the most probable $\widehat{q_{\mathrm{sat}}} - 4.5$ mm), and panels on the right displaying a high-$\widehat{q_{\mathrm{sat}}}$ bin (the most probable $\widehat{q_{\mathrm{sat}}} + 4.5$ mm).

The individual colored lines in Fig. 9a from PR precipitation represent $P \times \mathrm{Prob}(P|\mathrm{CWV} - w_c) \times \mathrm{Prob}(\mathrm{CWV} - w_c)$ for different values of CWV $- w_c$. The shape of the curve at moderate to high P is primarily determined by $\mathrm{Prob}(P|\mathrm{CWV} - w_c)$. These precipitation contributions vanish at zero because of P, which does not otherwise greatly alter the profiles of $\mathrm{Prob}(P|\mathrm{CWV} - w_c)$ for $P > 3\,\mathrm{mm\,h^{-1}}$. The lowest CWV $- w_c$ values only permit low P ($< 2\,\mathrm{mm\,h^{-1}}$). Around critical (yellow line), an approximately exponential tail may be noted above $P \sim 2\,\mathrm{mm\,h^{-1}}$ extending to the highest precipitation values for which sufficient data are available. The slope of this tail is insensitive to CWV $- w_c$ over a wide range (-9.6 to 4.8 mm). As CWV exceeds critical, the precipitation contribution develops a maximum at a positive P, which shifts slightly toward higher P with further

←

compiled using the hourly AM4G9 model output. (e)–(j) As in (c) and (d), but using the hourly output from the AM4B6, CAM5.3, and SPCAM, respectively.
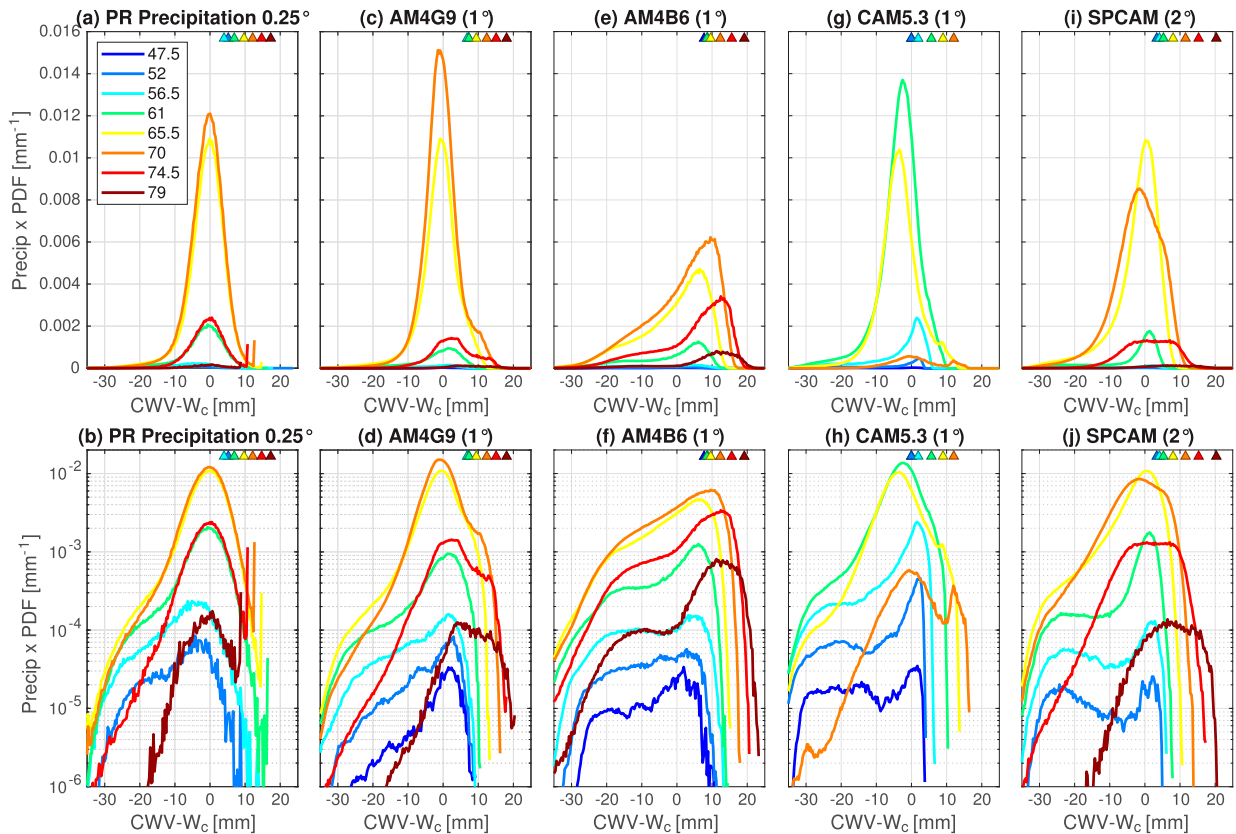
FIG. 10. (a) The precipitation contribution (i.e., precipitation-rate-weighted CWV PDF), on a linear scale, as a function of CWV relative to critical and $\widehat{q_{sat}}$ (colors) in the tropical WPac compiled at 0.25° using the PR 2A25 precipitation rate, TMIv7.1 CWV, and Reanalysis-2 temperature. Here the triangles represent the values of $\widehat{q_{sat}}$ relative to the critical CWV, which indicate where the column is approximately saturated. (b) As in (a), but on a $\log_{10}$ scale. (c)–(j) As in (a) and (b), but using the hourly output from the AM4G9, AM4B6, CAM5.3, and SPCAM.

increase in CWV [this evolution of maximum can also be seen in $\text{Prob}(P|\text{CWV} - w_c)$ and is more pronounced for higher spatial resolution; see KSN18]. At the highest $\text{CWV} - w_c$ (9.6 mm; red), the precipitation contribution exhibits a broad spread in P, indicating that strong precipitation is more frequent given very high CWV values. However, the contribution from the highest $\text{CWV} - w_c$ is only a small fraction of the overall contribution (gray), which roughly matches that at critical (yellow) because of the modulation by $\text{Prob}(\text{CWV} - w_c)$. The corresponding statistics in Fig. 9b are consistent with those in Fig. 9a but display a faster decay at high P caused by the (retrieval dependent) cutoff $\sim 10 \text{ mm h}^{-1}$ in the TMIv7.1 precipitation.

We evaluate the model-simulated precipitation contributions in Figs. 9c–j. For low $\widehat{q_{sat}}$ (Figs. 9c,e,g,i), the models capture some aspects of the observed dependence of precipitation on CWV to an extent that varies among models. For instance, the precipitation contribution drops rapidly for CWV below critical, and the contribution from high precipitation values increases with CWV. Around critical (yellow line), a

local maximum of the precipitation contribution can be seen at a positive P. This local maximum occurs at higher P with its magnitude decreasing as CWV further increases because of $\text{Prob}(\text{CWV} - w_c)$. The contributions tend to be less asymmetric in P around the local maximum compared to observations (especially for AM4B6, CAM5.3, and SPCAM). These less asymmetric contributions explain why the conditional average of precipitation tends to coincide with the median noted in Fig. 8.

Other departures from observations can also be noted. Each model exhibits some range that appears qualitatively consistent with an exponential tail toward high precipitation. However, the tail slope (in log Y coordinates), where it exists, varies substantially among models and does not quantitatively match observations. The tail slope ends to be shallower for higher $\text{CWV} - w_c$ values; that is, strong precipitation is more frequent given higher CWV. Comparing the low-$\widehat{q_{sat}}$ contributions to their high-$\widehat{q_{sat}}$ counterparts (Figs. 9d,f,h,j), high-$(\text{CWV} - w_c)$ events (red and brown) are more frequent for high $\widehat{q_{sat}}$, reflecting that there are more above critical evens as noted

in section 4a. Using the overall precipitation contribution (gray) as a reference, the high-$\widehat{q_{sat}}$ contributions tend to decay slower than the low-$\widehat{q_{sat}}$ ones. These indicate that both Prob(P|CWV $- w_c$) and Prob(CWV $- w_c$) exhibit spurious dependence on $\widehat{q_{sat}}$, inconsistent with observations.

Figure 10 shows the precipitation contribution from a different angle, that is, as a function of CWV $- w_c$ for different $\widehat{q_{sat}}$ bins, indicated by colors, for WPac, with the top row (bottom row) in a linear (log) Y scale. Here the area under each curve represents the precipitation contributed by each $\widehat{q_{sat}}$.

The observed contributions (Fig. 10a) for the most common $\widehat{q_{sat}}$ values peak around critical with a common near-Gaussian core (Fig. 10b). Variations can be noted for CWV below critical (< -15 mm), which clearly deviates from Gaussian, presumably affected by dry-regime dynamics and nonconvective rain. For low-$\widehat{q_{sat}}$ bins (≤ 56.5 mm), the contributions peak slightly below critical with a wider spread in CWV, contrasting tropical versus extratropical precipitation.

The precipitation contributions simulated by the AM4G9 (Figs. 10c,d) and SPCAM (Figs. 10i,j) also peak around critical but tend to shift and spread toward higher CWV relative to critical as $\widehat{q_{sat}}$ increases. For CAM5.3 (Figs. 10g,h), the contributions peak around critical but do not exhibit consistent dependence on $\widehat{q_{sat}}$, and the contribution for the highest $\widehat{q_{sat}}$ (70 mm) is bimodal, consistent with the CWV PDF in Fig. 4g. The greatest departure from observations are noted for the AM4B6 (Figs. 10e,f), with the contributions spreading across a wide range of CWV, and the peak clearly shifting with $\widehat{q_{sat}}$. These features display the dependence of precipitation on $\widehat{q_{sat}}$ that generally agree with Fig. 9. We note that the differences from observations are exhibited even around critical, near the peak of the distribution, and are thus likely to be robust to any retrieval issues at high precipitation.

Overall, the precipitation contributions in Figs. 9 and 10 show that the models exhibit many qualitative features of the observations, but also exhibit substantial quantitative deviations. These combine with biases in the PDF of CWV $- w_c$, in which the models overproduce above-critical events (especially at high temperature) to yield the errors in the joint PDF seen in Fig. 8.

6. Summary and discussion

Most of the models examined simulate some version of the observed precipitation pickup with CWV. However, significant intermodel spread and departures from observations in multiple aspects of the convective transition statistics suggest these provide a challenging

observational constraint. Examining these aspects separately using the 6-hourly and higher-frequency model output provides a comprehensive assessment for deep convective parameterizations with clues for improvements. Below we briefly summarize the comparisons of these aspects.

a. Precipitation pickup and CWV relative to critical

In observations, the conditionally averaged precipitation, as a function of CWV for a given bulk tropospheric temperature $\widehat{q_{sat}}$, sharply increase as CWV exceeds the critical threshold w_c (Fig. 1a). The value of w_c increases with $\widehat{q_{sat}}$ but the corresponding critical column RH $w_c/\widehat{q_{sat}}$ decreases (Figs. 1k,l). Offline calculations have suggested that the dependence of w_c and $w_c/\widehat{q_{sat}}$ on $\widehat{q_{sat}}$ is a generic consequence of including entrainment in the estimation of buoyancy in convective updraft (Sahany et al. 2012). The conditionally averaged precipitation exhibits little variation across ocean basin (Fig. 1i) and is insensitive to spatial averaging (KSN18). Furthermore, when viewed as a function of CWV $- w_c$, its functional form shows little dependence on $\widehat{q_{sat}}$ (Figs. 1e,i). This reaffirms the interpretation that CWV $- w_c$ combines the impacts of tropospheric moisture and temperature on conditional instability, through entrainment, into a single measure (Holloway and Neelin 2009; Schiro et al. 2016; KSN18).

Among the examined models, AM4B6 (Fig. 3a) satisfactorily simulates the conditionally averaged precipitation that exhibits modest sensitivity to $\widehat{q_{sat}}$ (Fig. 3e) and little variation across ocean basin (Fig. 3i). The corresponding critical values match observations (Figs. 3k,l). However, the conditionally averaged precipitation simulated by the other models (Figs. 2, 4, 5, and 6a), tends to exhibit sensitivity to $\widehat{q_{sat}}$ (Fig. 5e) and basins (Fig. 5i), or results in different critical values (Figs. 4k,l). Figure 6a further demonstrates a significant intermodel spread in the critical values (where the precipitation picks up) or in the functional form of precipitation. For instance, the precipitation in the ISUGCM fails to pick up, likely because of the lack of entrainment in its convective scheme. The precipitation in CWB-GFS shows a two-step pickup, likely results from a built-in precipitation trigger that explicitly depends on environment humidity.

Most models that can simulate a decent precipitation pickup also capture the observed qualitative dependence of critical values on $\widehat{q_{sat}}$ (w_c increases and $w_c/\widehat{q_{sat}}$ decreases; not shown), indicating that entrainment is the essential mechanism.

b. Probability of precipitation and drizzle problem

The observed conditional probability of precipitation (defined relative to a threshold of precipitation

rate P) also exhibits a sharp pickup for CWV around critical (Figs. 1b,f). Its functional form can be approximated using an error function with standard deviation ~4 (units: mm; not shown). Lower $\widehat{q_{\mathrm{sat}}}$, lower P threshold, and lower spatial resolution (at which the statistics are computed) all lead to higher values of conditional probability without altering its functional form; that is, the conditional probability curve would shift slightly toward lower CWV (KSN18). Like the conditional average, the conditional probability can also be expressed as a function of CWV $- w_c$, which exhibits little variation across the $\widehat{q_{\mathrm{sat}}}$ range and basins (Figs. 1f,j).

As an example, we consider two GFDL AM4 cases with different convective parameterizations, one among the best and one among the poorest simulations in this measure. In the AM4G9, the conditional probability of precipitation closely resembles the observed values with a slightly steeper pickup (Fig. 2b), which starts at lower CWV relative to critical (Fig. 2f vs Fig. 1f). It also exhibits modest variation across basins (Fig. 2j). The simulated conditional probability picking up at lower CWV relative to critical may result from and is consistent with the difference in the temporal resolution of P (hourly average for AM4G9 vs snapshot for satellite retrievals). Despite the superior performance of AM4B6 in simulating conditionally averaged precipitation, the conditional probability in AM4B6 deviates considerably from observations (Fig. 3b). The pickup of conditional probability is gentler and shows a clear dependence on $\widehat{q_{\mathrm{sat}}}$ (Fig. 3f), that is, higher probability of precipitation at low CWV relative to critical especially at high $\widehat{q_{\mathrm{sat}}}$, indicating a drizzle problem in a warm environment (see also the CNRM instances in Fig. 6). This contrast in AM4B6's ability to simulate conditional average and probability of precipitation serves as a reminder that different aspects of the convective transition statistics must be examined separately. Regarding the other models, the simulated conditional probability exhibits sensitivity to $\widehat{q_{\mathrm{sat}}}$ (Figs. 4f and 5f) and variation across basins (Figs. 4j and 5j), and even nonmonotonic behavior. Figure 6b shows a substantial intermodel spread and that the conditional probability in most models picks up at CWV values lower than observed, many of which cannot be explained by the difference in the temporal resolution of P alone.

c. PDF of CWV

The observed CWV PDFs have $\widehat{q_{\mathrm{sat}}}$-dependent characteristic shapes with two peaks/cutoffs at low and high CWV values (Fig. 1c), and are relatively insensitive to resolution. For low $\widehat{q_{\mathrm{sat}}}$, the PDF peaks at a low

CWV value above which the PDF decreases gradually until reaching a high-CWV cutoff right below critical (Fig. 1g). As $\widehat{q_{\mathrm{sat}}}$ increases, the high-CWV cutoff develops into a peak. The pickup of precipitation suggests that the behavior for CWV above critical is governed by the moist-regime dynamics, that is, conditional instability. Consequently, the (properly normalized) CWV PDF exhibits little variation across the $\widehat{q_{\mathrm{sat}}}$ range (Fig. 1g) and ocean basins (KSN18). Stochastic models suggested that the functional form of the CWV PDF in this regime is primarily controlled by precipitation removal balancing low-level convergence of moisture (Stechmann and Neelin 2011, 2014). In contrast, at low CWV, the PDF and fraction of nonprecipitating events vary considerably (Fig. 1g), suggesting other factors influencing the dry regime, for example, prevailing subsidence and extratropical events intruding into the tropics (KSN18).

For low $\widehat{q_{\mathrm{sat}}}$, the CWV PDFs are primarily determined by the dry-regime dynamics, and all the models simulate this aspect in reasonable agreement with observations (Figs. 2–5c,g and 7a). But when moist-regime dynamics becomes dominant as $\widehat{q_{\mathrm{sat}}}$ increases, the simulated CWV PDFs by many of the models depart from the observed (Figs. 7b,c); for example, the PDF has a broad spread around intermediate CWV values (CNRM cases). Some of the models overproduce very high-CWV events especially at high $\widehat{q_{\mathrm{sat}}}$ values (Figs. 3g and 5g), which may result from small gross moist stability during precipitation. Note that the CWV PDFs for highest $\widehat{q_{\mathrm{sat}}}$ values in the AM4G9 (Fig. 2g) and CAM5.3 (Fig. 4g) seemingly indicate more above-critical events, but still fall within the observational uncertainty.

d. PDF of CWV for precipitating events

The CWV PDF for precipitating events here is defined as the product of the CWV PDF and conditional probability. Consequently, it modestly depends on the P threshold and resolution. In observations, the CWV PDFs for precipitating events for $\widehat{q_{\mathrm{sat}}} \gtrsim 70$ mm display a common near-Gaussian core (Fig. 1h), indicating convection favors specific thermodynamic conditions with a narrow water vapor range. For lower $\widehat{q_{\mathrm{sat}}}$ values, the corresponding PDFs coincide with the high-$\widehat{q_{\mathrm{sat}}}$ PDFs for CWV around and above critical, but also indicate greater probability of precipitation given CWV below critical. The geographical distribution of $\widehat{q_{\mathrm{sat}}}$ suggests these low-$\widehat{q_{\mathrm{sat}}}$ below-critical precipitation occurrences are in part associated with extratropical events resulting from other mechanisms, for example, large-scale saturation (KSN18).

Among the examined models, the AM4G9 and CAM5.3 can reproduce the common near-Gaussian core to some

extent (Figs. 2h and 4h), but the contrast in below-critical precipitation for high versus low $\widehat{q_{\text{sat}}}$ is less pronounced as observed. The SPCAM, on the other hand, seems more capable of simulating this contrast but the PDF spreads over a broader range of CWV (Fig. 5h). The AM4B6 performs poorly in this regard (Fig. 3h) as a result of the biased CWV PDF and conditional probability (Figs. 3f,g). See also Fig. S1 for CWV PDFs in the MJOTF/GASS models.

e. Joint PDF of precipitation and CWV relative to critical

In observations, the joint PDF of P and CWV $- w_c$ exhibits an abrupt transition from the dry, nonprecipitating regime into the moist regime as CWV increases from below critical (Fig. 8a). In the moist regime, a robust exponential tail toward high precipitation can be noted in the PDF of P for CWV around critical (Fig. 9a), and the accumulated precipitation is mostly contributed by events in this regime (Figs. 10a,b). The slope of the exponential tail, and more generally, the PDF of P, depend on spatial averaging (KSN18). The joint PDF shows little variation across the $\widehat{q_{\text{sat}}}$ range ≥ 61 mm and ocean basins (KSN18).

The four models for which we examined joint PDFs with hourly data, AM4G9, AM4B6, CAM5.3 and SPCAM, can simulate the transition from the dry to moist regime to some extent (Figs. 8c–f). However, the simulated transitions are less abrupt than observed. High precipitation tends to occur at above-critical CWV values but is less likely for around- and below-critical CWV than in the observed. The CAM5.3 especially underestimates the variability of precipitation (Fig. 8e). At relatively low $\widehat{q_{\text{sat}}}$, the simulated PDFs of P seem to exhibit some version of the asymptotic tail into high precipitation (Figs. 9c,e,g,i). The tails at critical CWV drop more rapidly than observed. Moreover, the simulated tails display dependence on CWV and indicate that strong precipitation favors high $\widehat{q_{\text{sat}}}$, that is, a warm troposphere (Figs. 9d,f,h,j). These spurious dependencies on CWV and $\widehat{q_{\text{sat}}}$ lead to biased precipitation contribution. For instance, the above-critical contribution of precipitation at high $\widehat{q_{\text{sat}}}$ values is slightly exaggerated in the AM4G9 (Figs. 10c,d), and the AM4B6 precipitation is contributed over a broader range and mostly from above-critical CWV (Figs. 10e,f). This identifies the high-precipitation, high-CWV range as a regime demanding greater scrutiny as further discussed below.

f. Additional inferences based on the ensemble

Several comparisons are available in individual models with multiple instances differing in some specific components, permitting additional inferences regarding using the convective transition statistics as diagnostic tools:

1) Where the model (AM4 and CAM5.3 vs SPCAM) is available with alternative representations of moist convection, the statistics distinguish different instances in multiple aspects, despite all the model instances having been calibrated against typical diagnostic metrics.

2) Different cloud microphysics in the convective parameterizations in the same model (CAM5) only cause minor variations in the joint distribution of CWV and $\widehat{q_{\text{sat}}}$, but otherwise do not notably alter the statistics examined here.

3) Where the same model (CAM5) is examined at hourly and 6-hourly time averaging (of precipitation), the results are comparable. Although output at model time step or hourly time scale are preferable, the analysis can apply with more conventional subdaily output.

4) Where the model (CNRM and SPCAM) is available in uncoupled versus coupled versions, or with different forcing settings through the lower boundary, the major difference appears in the probability distribution of (CWV, $\widehat{q_{\text{sat}}}$) associated with climate drift caused by coupling/forcing configuration. Other aspects of the statistics, for example, the precipitation pickup and CWV PDF, are less sensitive.

These cases in this ensemble of opportunity further indicate that the convective transition statistics substantially discriminate between convective parameterizations and are reasonably robust to subdaily time averaging, that is, can be used with conventional model data.

g. Possible action items for model revision and diagnostic development

While these diagnostics help identify the relationship between tropical precipitation and its thermodynamic environment in considerable detail, the diagnostics presented here can lead to suggestions for specific revisions of a given convective parameterization. The link is not direct, however. Analysis and improvement necessarily involve specifics of each model's set of parameterizations and can involve interaction of these parameterizations with emergent behavior of the dynamics. While it is not possible to cover detailed analysis for each model in the ensemble, here we discuss process hypotheses and suggestions for further diagnostic development, broken out by type of error. These are all offered with the caveat that changes to improve model performance under one set of diagnostics can often

erode the performance under other measures (Kim et al. 2011; Langenbrunner and Neelin 2017).

1) ERRORS IN POSITION/SHAPE OF ONSET

For models exhibiting errors in the functional form of conditional precipitation, the leading candidate for adjustment can be the entrainment assumptions in the convective scheme, since these are known to impact the critical values simulated by models (Sahany et al. 2012) or even the existence of a sharp pickup in precipitation (Kuo et al. 2017). Plume calculations with higher entrainment are more sensitive to the free-tropospheric environmental humidity, resulting in precipitation tending to pick up at higher CWV. Changes in a vertically constant entrainment rate can impact circulation or vertical distribution of cloud (Mapes and Neale 2011; Qian et al. 2018; Schiro et al. 2019). Recent analysis of observations and reanalysis (Schiro et al. 2018; Ahmed and Neelin 2018) point to a large influence of the environment on convective plume through a deep lower-tropospheric layer contributing relatively uniformly to the updraft mass flux from all levels. This may be consistent with certain representations of entrainment (e.g., Siebesma et al. 2007), although if it occurs substantially through dynamical entrainment (Suselj et al. 2019) the strong effects may be confined to the lower troposphere.

This suggests that models that fail to simulate a strong precipitation pickup (e.g., ISUGCM) may benefit from increased lower-tropospheric entrainment. Some models in the ensemble exhibit a multistep pickup (CWB-GFS) because precipitation is triggered with respect to a certain humidity threshold. Apparently, this kind of trigger must be designed with caution to match the observed precipitation–moisture relationship and may not be necessary if entrainment is reasonably represented.

2) ERRORS IN WATER VAPOR/PRECIPITATION PDFS

(i) Errors in shape of water vapor PDF

The shape of the CWV PDF is largely controlled by the dominant moisture budget balance. Statistics from observations clearly distinguish between the wet, precipitating regime and the dry, nonprecipitating regime. The overprediction of drizzle frequency in some of the models can be thought of as a spurious sink term of moisture at low CWV, contributing to biases in CWV PDF. In the wet regime, a longer convective adjustment time scale can be a factor tending to limit the rate at which the convective scheme removes moisture. In response, the environment reaches saturation more often and results in a higher fraction of precipitation occurring

by gridscale condensation associated with convection (e.g., Jiang et al. 2016).

(ii) Too much precipitation below main onset (drizzle problem) and precipitating PDF too wide

Increasing entrainment can alleviate the drizzle problem over tropical oceans (but not over land, in CESM1; Kuo et al. 2017). Models produce precipitation through contributions by various parameterizations (e.g., cloud microphysics, shallow and deep convective) under different circumstances. Identifying precipitation types in varying thermodynamic conditions using radar rainfall products may help modelers coordinate parameterization schemes and quantify conditional instability given the tropospheric temperature–moisture state, for example, in terms of entraining CAPE or general cloud work functions.

(iii) Joint PDF follows conditionally averaged precipitation too closely and precipitation PDF/contribution tail errors at high precipitation

Several features of the joint PDF described in section 6e can be summarized as the model joint PDF tending to follow the pickup of the conditionally average precipitation, with smaller spread about this than in observations. This suggests that for a given thermodynamic environment, the precipitation is too deterministic. This is consistent with simulated extreme precipitation being improved by explicitly incorporating a stochastic component (Plant and Craig 2008; Wang et al. 2017). It could also be consistent with representation of additional sources of variability including effects of subgrid-scale moisture variability, gustiness, downdrafts, cold pools, or organized systems (e.g., Hourdin et al. 2013; Harrop et al. 2018; Mapes and Neale 2011).

The longer-than-Gaussian tail of the observed precipitation distribution/contribution at high P is insensitive to the bulk measures of water vapor and temperature in the retrieval datasets used here. Given the importance of model projections of changes in extreme precipitation under global warming, the departures of the model precipitation PDFs from the observed in the high-precipitation, high-CWV regime as a function of temperature is of concern. Independent observational datasets, for instance from radio occultation (Padullés et al. 2018), could be used to further constrain the behavior in this regime; process modeling could be used to better identify sources of differences among models; and this regime can be an important target for cloud-resolving models.

h. Concluding remarks

The statistics presented here are available as the convective transition diagnostic module associated with the

Model Diagnostics Task Force (MDTF) diagnostics package (Maloney et al. 2019b; available at http://www.cesm.ucar.edu/working_groups/Atmosphere/mdtf-diagnostics-package/index.html). As applied to the set of models analyzed here, the convective transition statistics summarized above reveal substantial departures from observations and intermodel spread, especially for CWV within the moist regime, reflecting the current status of model representations of moist convection and its interaction with the large-scale flow. Although several models performed poorly with respect to the measures introduced here, it is encouraging that for the basic statistics (i.e., pickup of precipitation and probability, CWV PDF and CWV PDF for precipitating points) a few cases—including AM4G9, EC-EARTH3, GEOS-5, and CAM5—performed well. This is particularly noteworthy as in almost all cases the models had not previously been assessed with respect to these measures so have clearly not been in any way tuned to achieve these results. For a model to do well, the parameterization must reasonably capture multiple aspects of the triggering of deep convection associated with conditional instability. From related work, there is evidence that this requires a reasonable representation of the dependence on lower free-tropospheric humidity by entrainment into the deep convective plumes. It also implies that the parameterization of convective heating as a function of buoyancy is operating well, and that the overall effects in the model yielding large-scale variations with which the convection interacts are of a suitable magnitude—on the one hand driving the system into the high-moisture, high-precipitation regime, and on the other causing event (i.e., precipitation) termination—with each occurring at a reasonable frequency. However, even in models that perform well, the high-temperature, high-CWV, high-precipitation regime is flagged as challenging to simulate in detailed comparison to the observations at these fast time scales.

REFERENCES

Ahmed, F., and J. D. Neelin, 2018: Reverse engineering the tropical precipitation–buoyancy relationship. *J. Atmos. Sci.*, **75**, 1587–1608, https://doi.org/10.1175/JAS-D-17-0333.1.

Annamalai, H., J. Hafner, A. Kumar, and H. Wang, 2014: A framework for dynamical seasonal prediction of precipitation over the Pacific Islands. *J. Climate*, **27**, 3272–3297, https://doi.org/10.1175/JCLI-D-13-00379.1.

Bao, Q., and Coauthors, 2013: The flexible global ocean-atmosphere-land system model, spectral version 2: FGOALS-s2. *Adv. Atmos. Sci.*, **30**, 561–576, https://doi.org/10.1007/s00376-012-2113-9.

Biasutti, M., 2013: Forced Sahel rainfall trends in the CMIP5 archive. *J. Geophys. Res. Atmos.*, **118**, 1613–1623, https://doi.org/10.1002/jgrd.50206.

——, and A. H. Sobel, 2009: Delayed Sahel rainfall and global seasonal cycle in a warmer climate. *Geophys. Res. Lett.*, **36**, L23707, https://doi.org/10.1029/2009GL041303.

Bitz, C. M., and Coauthors, 2012: Climate sensitivity of the Community Climate System Model, version 4. *J. Climate*, **25**, 3053–3070, https://doi.org/10.1175/JCLI-D-11-00290.1.

Covey, C., P. J. Gleckler, C. Doutriaux, D. N. Williams, A. Dai, J. Fasullo, K. Trenberth, and A. Berg, 2016: Metrics for the diurnal cycle of precipitation: Toward routine benchmarks for climate models. *J. Climate*, **29**, 4461–4471, https://doi.org/10.1175/JCLI-D-15-0664.1.

Dai, A., 2006: Precipitation characteristics in eighteen coupled climate models. *J. Climate*, **19**, 4605–4630, https://doi.org/10.1175/JCLI3884.1.

Del Genio, A. D., and J. Wu, 2010: The role of entrainment in the diurnal cycle of continental convection. *J. Climate*, **23**, 2722–2738, https://doi.org/10.1175/2009JCLI3340.1.

——, Y. Chen, D. Kim, and M.-S. Yao, 2012: The MJO transition from shallow to deep convection in *CloudSat*/CALIPSO and GISS GCM simulations. *J. Climate*, **25**, 3755–3770, https://doi.org/10.1175/JCLI-D-11-00384.1.

Donner, L. J., 1993: A cumulus parameterization including mass fluxes, vertical momentum dynamics, and mesoscale effects. *J. Atmos. Sci.*, **50**, 889–906, https://doi.org/10.1175/1520-0469(1993)050<0889:ACPIMF>2.0.CO;2.

——, and Coauthors, 2011: The dynamical core, physical parameterizations, and basic simulation characteristics of the atmospheric component AM3 of the GFDL Global Coupled Model CM3. *J. Climate*, **24**, 3484–3519, https://doi.org/10.1175/2011JCLI3955.1.

Eyring, V., and Coauthors, 2019: Taking climate model evaluation to the next level. *Nat. Climate Change*, **9**, 102–110, https://doi.org/10.1038/s41558-018-0355-y.

Forbes, R., A. Tompkins, and A. Untch, 2012: A new prognostic bulk microphysics scheme for the IFS. ECMWF Tech. Memo. 649, 30 pp.

Gonzalez, A., and X. Jiang, 2017: Winter mean lower-tropospheric moisture over the Maritime Continent as a Climate model diagnostic metric for the propagation of the Madden-Julian oscillation. *Geophys. Res. Lett.*, **44**, 2588–2596, https://doi.org/10.1002/2016GL072430.

Harrop, B. E., and Coauthors, 2018: The role of convective gustiness in reducing seasonal precipitation biases in the tropical west Pacific. *J. Adv. Model. Earth Syst.*, **10**, 961–970, https://doi.org/10.1002/2017MS001157.

Harshvardhan, R. Davies, D. A. Randall, and T. G. Corsetti, 1987: A fast radiation parameterization for atmospheric circulation models. *J. Geophys. Res.*, **92**, 1009–1016, https://doi.org/10.1029/JD092iD01p01009.

Hazeleger, W., and Coauthors, 2012: EC-EARTH v2.2: Description and validation of a new seamless Earth system prediction model. *Climate Dyn.*, **39**, 2611–2629, https://doi.org/10.1007/s00382-011-1228-5.

Henderson, S. A., E. D. Maloney, and S.-W. Son, 2017: Madden–Julian oscillation teleconnections: The impact of the basic state and MJO representation in general circulation models. *J. Climate*, **30**, 4567–4587, https://doi.org/10.1175/JCLI-D-16-0789.1.

Hirota, H., Y. N. Takayabu, M. Watanabe, M. Kimoto, and M. Chikira, 2014: Role of convective entrainment in spatial distributions of and temporal variations in precipitation over tropical oceans. *J. Climate*, **27**, 8707–8723, https://doi.org/10.1175/JCLI-D-13-00701.1.

Hogan, T. F., and Coauthors, 2014: The Navy Global Environmental Model. *Oceanography*, **27** (3), 116–125, https://doi.org/10.5670/oceanog.2014.73.

Holloway, C. E., and J. D. Neelin, 2009: Moisture vertical structure, column water vapor, and tropical deep convection. *J. Atmos. Sci.*, **66**, 1665–1683, https://doi.org/10.1175/2008JAS2806.1.

Hourdin, F., and Coauthors, 2013: LMDZ5B: The atmospheric component of the IPSL climate model with revisited parameterizations for clouds and convection. *Climate Dyn.*, **40**, 2193–2222, https://doi.org/10.1007/s00382-012-1343-y.

Hwang, Y.-T., and D. M. W. Frierson, 2013: Link between the double-intertropical convergence zone problem and cloud biases over the Southern Ocean. *Proc. Natl. Acad. Sci. USA*, **110**, 4935–4940, https://doi.org/10.1073/pnas.1213302110.

Jiang, X., 2017: Key processes for the eastward propagation of the Madden-Julian oscillation based on multi-model simulations. *J. Geophys. Res. Atmos.*, **122**, 755–770, https://doi.org/10.1002/2016JD025955.

——, and Coauthors, 2015: Vertical structure and physical processes of the Madden-Julian oscillation: Exploring key model physics in climate simulations. *J. Geophys. Res. Atmos.*, **120**, 4718–4748, https://doi.org/10.1002/2014JD022375.

——, M. Zhao, E. Maloney, and D. E. Waliser, 2016: Convective moisture adjustment time-scale as a key factor in regulating model amplitude of the Madden-Julian oscillation. *Geophys. Res. Lett.*, **43**, 10 412–10 419, https://doi.org/10.1002/2016GL070898.

Kanamitsu, M., and Coauthors, 2002: NCEP/DOE AMIP-II reanalysis (R-2). *Bull. Amer. Meteor. Soc.*, **83**, 1631–1643, https://doi.org/10.1175/BAMS-83-11-1631.

Khairoutdinov, M. F., and D. A. Randall, 2003: Cloud resolving modeling of the ARM summer 1997 IOP: Model formulation, results, uncertainties, and sensitivities. *J. Atmos. Sci.*, **60**, 607–625, https://doi.org/10.1175/1520-0469(2003)060<0607:CRMOTA>2.0.CO;2.

Kim, D., A. H. Sobel, E. D. Maloney, D. M. Frierson, and I. Kang, 2011: A systematic relationship between intraseasonal variability

and mean state bias in AGCM simulations. *J. Climate*, **24**, 5506–5520, https://doi.org/10.1175/2011JCLI4177.1.

——, and Coauthors, 2014: Process-oriented MJO simulation diagnostic: Moisture sensitivity of simulated convection. *J. Climate*, **27**, 5379–5395, https://doi.org/10.1175/JCLI-D-13-00497.1.

——, and Coauthors, 2018: Process-oriented diagnosis of tropical cyclones in high-resolution GCMs. *J. Climate*, **31**, 1685–1702, https://doi.org/10.1175/JCLI-D-17-0269.1.

Kuo, Y.-H., J. D. Neelin, and C. R. Mechoso, 2017: Tropical convective transition statistics and causality in the water vapor-precipitation relation. *J. Atmos. Sci.*, **74**, 915–931, https://doi.org/10.1175/JAS-D-16-0182.1.

——, K. A. Schiro, and J. D. Neelin, 2018: Convective transition statistics over tropical oceans for climate model diagnostics: Observational baseline. *J. Atmos. Sci.*, **75**, 1553–1570, https://doi.org/10.1175/JAS-D-17-0287.1.

Kuo, K.-T., W.-T. Chen, and C.-M. Wu, 2019: Effects of convection-SST interactions on South China Sea summer monsoon onset in a multiscale modeling framework model. *Terr. Atmos. Ocean. Sci.*, https://doi.org/10.3319/TAO.2019.08.16.01, in press.

Langenbrunner, B., and J. D. Neelin, 2017: Multiobjective constraints for climate model parameter choices: Pragmatic Pareto fronts in CESM1. *J. Adv. Model. Earth Syst.*, **9**, 2008–2026, https://doi.org/10.1002/2017MS000942.

Liou, C. S., and Coauthors, 1997: The second-generation global forecast system at the Central Weather Bureau in Taiwan. *Wea. Forecasting*, **12**, 653–663, https://doi.org/10.1175/1520-0434-12.3.653.

Maloney, E. D., A. F. Adames, and H. X. Bui, 2019a: Madden-Julian oscillation changes under anthropogenic warming. *Nat. Climate Change*, **9**, 26–33, https://doi.org/10.1038/s41558-018-0331-6.

——, and Coauthors, 2019b: Process-oriented evaluation of climate and weather forecasting models. *Bull. Amer. Meteor. Soc.*, **100**, 1665–1686, https://doi.org/10.1175/BAMS-D-18-0042.1.

Mapes, B., and R. Neale, 2011: Parameterizing convective organization to escape the entrainment dilemma. *J. Adv. Model. Earth Syst.*, **3**, M06004, https://doi.org/10.1029/2011MS000042.

Merryfield, W. J., and Coauthors, 2013: The Canadian Seasonal to Interannual Prediction System. Part I: Models and Initialization. *Mon. Wea. Rev.*, **141**, 2910–2945, https://doi.org/10.1175/MWR-D-12-00216.1.

Molod, A. L., and Coauthors, 2012: The GEOS-5 atmospheric general circulation model: Mean climate and development from MERRA to Fortuna. NASA Tech. Rep. NASA TM-2012-104606, Vol. 28, 117 pp.

Morcrette, J. J., H. W. Barker, J. N. Cole, M. J. Iacono, and R. Pincus, 2008: Impact of a new radiation package, McRad, in the ECMWF integrated forecasting system. *Mon. Wea. Rev.*, **136**, 4773–4798, https://doi.org/10.1175/2008MWR2363.1.

Neale, R. B., J. H. Richter, and M. Jochum, 2008: The impact of convection on ENSO: From a delayed oscillator to a series of events. *J. Climate*, **21**, 5904–5924, https://doi.org/10.1175/2008JCLI2244.1.

——, and Coauthors, 2012: Description of the NCAR Community Atmosphere Model (CAM 5.0). NCAR Tech. Note NCAR/TN-486+STR, 289 pp., http://www.cesm.ucar.edu/models/cesm1.0/cam/docs/description/cam5_desc.pdf.

Neelin, J. D., O. Peters, and K. Hales, 2009: The transition to strong convection. *J. Atmos. Sci.*, **66**, 2367–2384, https://doi.org/10.1175/2009JAS2962.1.

Oueslati, B., and G. Bellon, 2013: Convective entrainment and large-scale organization of tropical precipitation: Sensitivity of the CNRM-CM5 hierarchy of models. *J. Climate*, **26**, 2931–2946, https://doi.org/10.1175/JCLI-D-12-00314.1.

Padullés, R., and Coauthors, 2018: Assessment of Global Navigation Satellite System (GNSS) radio occultation refractivity under heavy precipitation. *Atmos. Chem. Phys.*, **18**, 11 697–11 708, https://doi.org/10.5194/acp-18-11697-2018.

Petch, J. D., and Coauthors, 2011: A global model intercomparison of the physical processes associated with the MJO. *GEWEX News*, Vol. 21, No. 3, International GEWEX Project Office, Silver Spring, MD, 3–5.

Peters, O., and J. D. Neelin, 2006: Critical phenomena in atmospheric precipitation. *Nat. Phys.*, **2**, 393–396, https://doi.org/10.1038/nphys314.

Plant, R. S., and G. C. Craig, 2008: A stochastic parameterization for deep convection based on equilibrium statistics. *J. Atmos. Sci.*, **65**, 87–105, https://doi.org/10.1175/2007JAS2263.1.

Qian, Y., and Coauthors, 2018: Parametric sensitivity and uncertainty quantification in the version 1 of E3SM atmosphere model based on short perturbed parameter ensemble simulations. *J. Geophys. Res. Atmos.*, **123**, 13 046–13 073, https://doi.org/10.1029/2018JD028927.

Richter, J. H., and P. J. Rasch, 2008: Effects of convective momentum transport on the atmospheric circulation in the Community Atmosphere Model, version 3. *J. Climate*, **21**, 1487–1499, https://doi.org/10.1175/2007JCLI1789.1.

Rio, C., F. Hourdin, J.-Y. Grandpeix, and J.-P. Lafore, 2009: Shifting the diurnal cycle of parameterized deep convection over land. *Geophys. Res. Lett.*, **36**, L07809, https://doi.org/10.1029/2008GL036779.

Sahany, S., J. D. Neelin, K. Hales, and R. B. Neale, 2012: Temperature–moisture dependence of the deep convective transition as a constraint on entrainment in climate models. *J. Atmos. Sci.*, **69**, 1340–1358, https://doi.org/10.1175/JAS-D-11-0164.1.

——, ——, ——, and ——, 2014: Deep convective transition characteristics in the Community Climate System Model and changes under global warming. *J. Climate*, **27**, 9214–9232, https://doi.org/10.1175/JCLI-D-13-00747.1.

Schiro, K. A., and J. D. Neelin, 2019: Deep convective organization, moisture vertical structure, and convective transition using deep-inflow mixing. *J. Atmos. Sci.*, **76**, 965–987, https://doi.org/10.1175/JAS-D-18-0122.1.

——, ——, D. K. Adams, and B. R. Lintner, 2016: Deep convection and column water vapor over tropical land versus tropical ocean: A comparison between the Amazon and the tropical western Pacific. *J. Atmos. Sci.*, **73**, 4043–4063, https://doi.org/10.1175/JAS-D-16-0119.1.

——, F. Ahmed, S. E. Giangrande, and J. D. Neelin, 2018: GoAmazon2014/5 points to deep-inflow approach to mesoscale-organized and unorganized deep convection. *Proc. Natl. Acad. Sci. USA*, **115**, 4577–4582, https://doi.org/10.1073/pnas.1719842115.

——, and Coauthors, 2019: Relationships between tropical ascent and high cloud fraction changes with warming revealed by perturbation physics experiments in CAM5. *Geophys. Res. Lett.*, **46**, 10 112–10 121, https://doi.org/10.1029/2019GL083026.

Schmidt, G. A., and Coauthors, 2014: Configuration and assessment of the GISS ModelE2 contributions to the CMIP5 archive. *J. Adv. Model. Earth Syst.*, **6**, 141–184, https://doi.org/10.1002/2013MS000265.

Siebesma, A. P., P. M. M. Soares, and J. Teixeira, 2007: A combined eddy-diffusivity mass-flux approach for the convective boundary layer. *J. Atmos. Sci.*, **64**, 1230–1248, https://doi.org/10.1175/JAS3888.1.

Song, X., and G. J. Zhang, 2011: Microphysics parameterization for convective clouds in a global climate model: Description and single-column model tests. *J. Geophys. Res.*, **116**, D02201, https://doi.org/10.1029/2010JD014833.

Stechmann, S. N., and J. D. Neelin, 2011: A stochastic model for the transition to strong convection. *J. Atmos. Sci.*, **68**, 2955–2970, https://doi.org/10.1175/JAS-D-11-028.1.

——, and ——, 2014: First-passage-time prototypes for precipitation statistics. *J. Atmos. Sci.*, **71**, 3269–3291, https://doi.org/10.1175/JAS-D-13-0268.1.

Su, H., and Coauthors, 2017: Tightening of tropical ascent and high clouds key to precipitation change in a warmer climate. *Nat. Commun.*, **8**, 15771, https://doi.org/10.1038/ncomms15771.

Suselj, K., M. J. Kurowski, and J. Teixeira, 2019: On the factors controlling the development of shallow convection in eddy-diffusivity/mass-flux models. *J. Atmos. Sci.*, **76**, 433–456, https://doi.org/10.1175/JAS-D-18-0121.1.

Suzuki, K., and Coauthors, 2015: Evaluation of the warm rain formation process in global models with satellite observations. *J. Atmos. Sci.*, **72**, 3996–4014, https://doi.org/10.1175/JAS-D-14-0265.1.

TRMM, 2011: TRMM Precipitation Radar rainfall rate and profile L2 1.5 hours V7. GES DISC, accessed 19 August 2016, https://disc.gsfc.nasa.gov/datacollection/TRMM_2A25_7.html.

Voigt, A., and Coauthors, 2016: The tropical rain belts with an annual cycle and a continent model intercomparison project: TRACMIP. *J. Adv. Model. Earth Syst.*, **8**, 1868–1891, https://doi.org/10.1002/2016MS000748.

Voldoire, A. E., and Coauthors, 2013: The CNRM-CM5.1 global climate model: Description and basic evaluation. *Climate Dyn.*, **40**, 2091–2121, https://doi.org/10.1007/s00382-011-1259-y.

Wang, Y., G. J. Zhang, and Y. He, 2017: Simulation of precipitation extremes using a stochastic convective parameterization in the NCAR CAM5 under different resolutions. *J. Geophys. Res. Atmos.*, **122**, 12 875–12 891, https://doi.org/10.1002/2017JD026901.

Watanabe, M. T., and Coauthors, 2010: Improved climate simulation by MIROC5: Mean states, variability, and climate sensitivity. *J. Climate*, **23**, 6312–6335, https://doi.org/10.1175/2010JCLI3679.1.

Wentz, F. J., C. Gentemann, and K. A. Hilburn, 2015: Remote Sensing Systems TRMM TMI daily environmental suite on 0.25 deg grid, version 7.1. Remote Sensing Systems, accessed 8 July 2016, www.remss.com/missions/tmi.

Wing, A. A., and K. A. Emanuel, 2014: Physical mechanisms controlling self-aggregation of convection in idealized numerical modeling simulations. *J. Adv. Model. Earth Syst.*, **6**, 59–74, https://doi.org/10.1002/2013MS000269.

Wu, T., and Coauthors, 2010: The Beijing Climate Center atmospheric general circulation model: Description and its performance for the present day climate. *Climate Dyn.*, **34**, 123–147, https://doi.org/10.1007/s00382-008-0487-2.

Wu, X., and L. Deng, 2013: Comparison of moist static energy and budget between the GCM-simulated Madden–Julian oscillation and observations over the Indian Ocean and western Pacific. *J. Climate*, **26**, 4981–4993, https://doi.org/10.1175/JCLI-D-12-00607.1.

Yukimoto, S. Y., and Coauthors, 2012: A new global climate model of the Meteorological Research Institute: MRI-CGCM3—Model

description and basic performance. *J. Meteor. Soc. Japan*, **90A**, 23–64, https://doi.org/10.2151/jmsj.2012-A02.

Zhang, G. J., and N. A. McFarlane, 1995: Sensitivity of climate simulations to the parameterization of cumulus convection in the Canadian Climate Centre general circulation model. *Atmos.–Ocean*, **33**, 407–446, https://doi.org/10.1080/07055900.1995.9649539.

Zhao, M., I. M. Held, S.-J. Lin, and G. A. Vecchi, 2009: Simulations of global hurricane climatology, interannual variability, and response to global warming using a 50-km resolution GCM. *J. Climate*, **22**, 6653–6678, https://doi.org/10.1175/2009JCLI3049.1.

——, and Coauthors, 2018a: The GFDL global atmosphere and land model AM4.0/LM4.0: 1. Simulation characteristics with prescribed SSTs. *J. Adv. Model. Earth Syst.*, **10**, 691–734, https://doi.org/10.1002/2017MS001208.

——, and Coauthors, 2018b: The GFDL global atmosphere and land model AM4.0/LM4.0: 2. Model description, sensitivity studies, and tuning strategies. *J. Adv. Model. Earth Syst.*, **10**, 735–769, https://doi.org/10.1002/2017MS001209.

Zhu, H., and H. Hendon, 2015: Role of large-scale moisture advection for simulation of the MJO with increased entrainment. *Quart. J. Roy. Meteor. Soc.*, **141**, 2127–2136, https://doi.org/10.1002/qj.2510.